A Pan-respiratory Antiviral Chemotype Targeting a Transient Host Multiprotein Complex

Authors: Andreas Müller-Schiffmann[1], Maya Michon[2], Anuradha F. Lingappa[2], Shao Feng Yu[2], Li Du[3], Fred Deiter[4], Sean Broce[2], Suguna Mallesh[2], Jackelyn Crabtree[5], Usha F. Lingappa[2], Amanda Macieik[2], Lisa Müller[6], Philipp Niklas Ostermann[6], Marcel Andrée[6], Ortwin Adams[6], Heiner Schaal[6], Robert J. Hogan[5], Ralph A. Tripp[5], Umesh Appaiah[2], Sanjeev K. Anand[7], Thomas W. Campi[7], Michael J. Ford[8], Jonathan C. Reed[9], Jim Lin[2], Olayemi Akintunde[2], Kiel Copeland[2], Christine Nichols[2], Emma Petrouski[2], A. Raquel Moreira[2], I-ting Jiang[2], Nicholas DeYarman[2], Ian Brown[2], Sharon Lau[2], Ilana Segal[2], Danielle Goldsmith[2], Shi Hong[2], Vinod Asundi[2], Erica M. Briggs[2], Ngwe Sin Phyo[2], Markus Froehlich[2], Bruce Onisko[10], Kent Matlack[2], Debendranath Dey[2], Jaisri R. Lingappa[9], M. Dharma Prasad[2], Anatoliy Kitaygorodskyy[2], Dennis Solas[2], Homer Boushey[11], John Greenland[4,11], Satish Pillai[3,11], Michael K. Lo[12], Joel M. Montgomery[12], Christina F. Spiropoulou[12], Carsten Korth[1], Suganya Selvarajah[2], Kumar Paulvannan[2], and Vishwanath R. Lingappa[2,11]*

Affiliations:

[1] Institute of Neuropathology, Heinrich Heine University, Düsseldorf, Germany.

[2] Prosetta Biosciences, San Francisco, CA, USA.

[3] Vitalant Research Institute, San Francisco, CA, USA.

[4] Veterans Administration Medical Center, San Francisco, CA, USA

[5] University of Georgia, Animal Health Research Center, Athens, GA, USA.

[6] Institute of Virology, Heinrich Heine University, Düsseldorf, Germany.

[7] Santo Biotech, LLC., Pendleton, IN, USA.

[8] MS Bioworks, Ann Arbor, MI, USA.

[9] Dept. of Global Health, University of Washington, Seattle, WA, USA.

[10] Onipro LLC., Kensington, CA, USA.

[11] University of California, San Francisco, CA, USA.

[12] Viral Special Pathogens Branch, US Centers for Disease Control and Prevention, Atlanta, GA, USA

* To whom correspondence should be addressed: vlingappa@prosetta.com

Abstract:

We present a small molecule chemotype, identified by an orthogonal drug screen, exhibiting nanomolar activity against members of all the six viral families causing most human respiratory viral disease, with a demonstrated barrier to resistance development. Antiviral activity is shown in mammalian cells, including human primary bronchial epithelial cells cultured to an air-liquid interface and infected with SARS-CoV-2. In animals, efficacy of early compounds in the lead series is shown by survival (for a coronavirus) and viral load (for a paramyxovirus). The drug target is shown to include a subset of the protein 14-3-3 within a transient host multi-protein complex containing components implicated in viral lifecycles and in innate immunity. This multi-protein complex is modified upon viral infection and largely restored by drug treatment. Our findings suggest a new clinical therapeutic strategy for early treatment upon upper respiratory viral infection to prevent progression to lower respiratory tract or systemic disease.

One Sentence Summary:

A host-targeted drug to treat all respiratory viruses without viral resistance development.

Introduction

The current SARS-CoV-2 pandemic has been characterized by waves of infection involving emerging mutants with varying degrees of resistance to current vaccines and treatments, confounded by waning immune responses. The risk of a new pandemic, as from high pathogenicity avian influenza or other viruses transmitted first from an animal reservoir to humans and then from human to humans, is ever present (European Food Safety Authority, European Centre for Disease Prevention, Control, European Union Reference Laboratory for Avian Influenza et al., 2021). Here we report findings suggesting an alternative antiviral approach involving an orally bioavailable small molecule drug directed to a novel host multi-protein complex target that is modified by members of the major viral families causing human respiratory tract disease. This chemotype is shown to avoid viral resistance development and would enable early treatment, at the onset of upper respiratory tract symptoms (e.g. a sore throat), to prevent progression to serious lower respiratory and/or systemic disease, regardless of the virus.

Viruses are recognized as challenging adversaries for two very different reasons. First, their small genomes mandate a reproductive strategy that involves reprogramming host protein machinery to meet viral needs rather than host homeostasis (Goodwin et al., 2015). This also means that there are relatively few virus-specific drug targets; all other targets (i.e. host machinery) have been presumed to have a high intrinsic risk of host toxicity. The second reason that antiviral therapeutics is challenging is that viral generation time is so much shorter than ours. This allows viruses, particularly RNA viruses, to rapidly evolve mutants that are resistant to virus-targeted therapies, including vaccines or drugs (Ison, 2011; Peck and Lauring, 2018).

A subset of antiviral targets represent an overlap between the virus and the host: the points of protein-protein interaction between the forementioned viral and host target classes (Andrei et al., 2017; Goodacre et al., 2020). Such targets have been historically difficult to identify and even harder to drug. However, the reproductive strategy of viruses also presents an opportunity to detect targets that are relatively inaccessible to conventional drug discovery methods. Over eons of time, viral evolution has selected for the most valuable of innumerable potential host targets and refined the best approach to

reprogramming those targets to meet the needs of the virus (Koonin et al., 2015; Krupovic and Koonin, 2017). In so doing, viruses have exploited features of our biology that we have yet to discover, including detection of targets not accessible to conventional proteomics (Aslam et al., 2017). It occurred to us that it might be possible to interrogate viruses in a manner that would reveal host targets not detected by current methods. Towards this end, we adapted the methods of cell-free protein synthesis and assembly (CFPSA), a variation on the tool by which the genetic code was deciphered (Nirenberg, 2004) and by which protein trafficking was deconvoluted (Blobel, 2000), to functionally reconstitute the transient virus-host protein-protein interactions culminating in viral capsid assembly (Lingappa et al., 1997, 1994; Lingappa and Lingappa, 2005). The CFPSA system was used to establish a phenotypic screen of drug-like small molecules for disruption of those protein-protein interactions to the detriment of the virus, as validated by their inhibition of replication of infectious virus in mammalian cell culture (Lingappa et al., 2013; Reed et al., 2021) and efficacy in animals.

Results

Discovery of antiviral compounds active across respiratory viral families

A body of literature suggests that viral capsid formation is catalyzed by host factors (Lingappa et al., 2021, 1997, 2013; Reed et al., 2021). Much of this prior work involved CFPSA systems programmed with mRNA encoding viral capsid proteins. A moderate throughput phenotypic drug screen involving CFPSA of influenza (FLUV) encoded proteins was developed (Petsch et al., 2010), analogous to what has also been done for rabies (Lingappa et al., 2013), HIV (Copeland et al., 2010; Reed et al., 2021), and other viruses (Broce et al., 2016). This screen is carried out in cellular extracts rather than in living cells, with formation of multimeric capsid protein complexes as a quantifiable, functional endpoint (Harrell, E.K.T. et al., 2010). Thus, the screen identified compounds that interfere with the biochemical pathway of host-catalyzed capsid assembly. Compounds identified as active by this method have therefore been termed *assembly modulators*. Three structurally unrelated assembly modulator hits were corroborated to be active against infectious FLUV in mammalian cells and advanced by structure-activity-relationship

optimization towards analogs demonstrating progressively higher antiviral activity with reduced cellular toxicity (Figure 1). One of these chemotypes was further advanced and is the focus of the studies reported here.

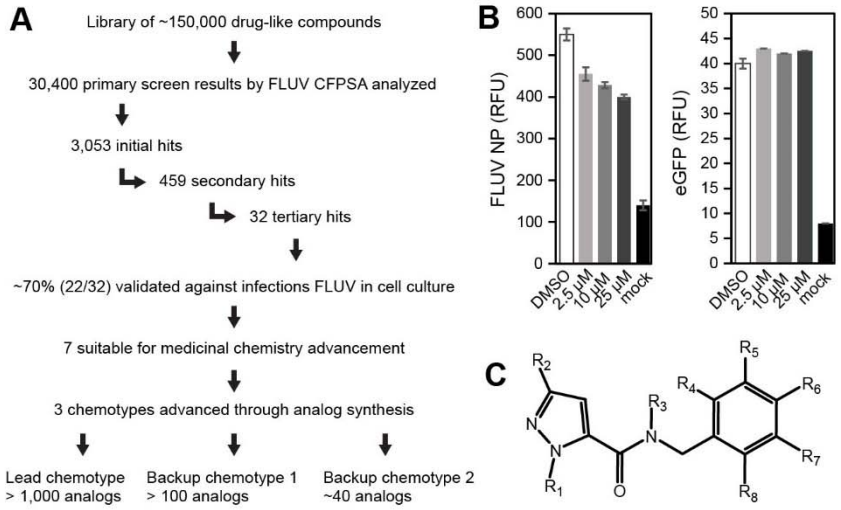

D

compound	R_1	R_2	R_3	R_4	R_5	R_6	R_7	R_8	EC_{90}(µM)
PAV-770	Me	t-Bu	H	O-CH_2-	CH_2-O-	H	F	H	1 - 3
PAV-868	Me	t-Bu	H	OMe	OMe	OMe	H	H	> 3
PAV-858	Me	t-Bu	H	OMe	H	OMe	OMe	H	> 3
PAV-772	Me	t-Bu	H	OMe	F	H	F	H	3
PAV-736	CH_2CH_2OH	t-Bu	H	OMe	OMe	H	H	H	> 3
PAV-869	Me	t-Bu	H	OPr	OMe	H	H	H	> 3
PAV-773	Me	t-Bu	H	OMe	OMe	H	H	H	< 1
PAV-1866	Me	t-Bu	Me	OMe	OMe	H	H	H	> 3
PAV-834	Me	Me	H	OMe	OMe	H	H	H	3
PAV-854	Me	Cy-hex	H	OMe	OMe	H	H	H	> 1
PAV-530	Me	iPr	H	OMe	OMe	H	H	H	1
PAV-835	Me	cyPr	H	OMe	OMe	H	H	H	< 1
PAV-895	Me	cyPr	H	OMe	Me	H	H	H	2
PAV-039	Me	cyPr	H	OMe	OMe	H	H	F	1
PAV-896	Me	cyPr	H	Me	OMe	H	H	H	1.5
PAV-700	Me	cyPr	H	Cl	OMe	H	H	H	2
PAV-235	Me	cyPr	H	F	OMe	H	H	H	0.2
PAV-944	Me	cyPr	H	OMe	CF_3	H	H	H	0.2
PAV-901	Me	cyPr	H	CF_3	OMe	H	H	H	0.3
PAV-671	Me	cyPr	H	H	Cl	OCF_3	H	H	0.05
PAV-774	Me	cyPr	H	Cl	OCF_3	H	H	H	0.2
PAV-431	Me	cyPr	H	OMe	OCF_3	H	H	H	< 0.1
PAV-528	Me	cyPr	H	$OCHF_2$	$OCHF_2$	H	H	H	< 0.1
PAV-877	Me	cyPr	H	H	Me	$OCHF_2$	Me	H	> 2

Legend to Figure 1. A. Output of the moderate throughput CFPSA screen involving FLUV nucleoprotein, culminating in three chemotypes validated against infectious virus, one of which was most extensively advanced and is presented here. B. Initial hit (PAV-770) of this chemotype in the plate screen showing dose-dependent titration of FLUV RFUs (left, reflecting inhibition of np multimerization/assembly) with no effect on eGFP RFUs (right, reflecting inhibition of protein synthesis).

C. Markush structure of the lead series. D. Initial structure-activity relationship based on assessment of FLUV infectivity in MDCK cells treated with these analogs.

Early promising compounds were counter-screened in mammalian cells against members of several unrelated viral families causing respiratory disease including human rhinovirus (HRV) bovine coronavirus (BoCoV), and murine herpesvirus (MHV), and were found to have activity comparable to that observed for FLUV (Figure 2).

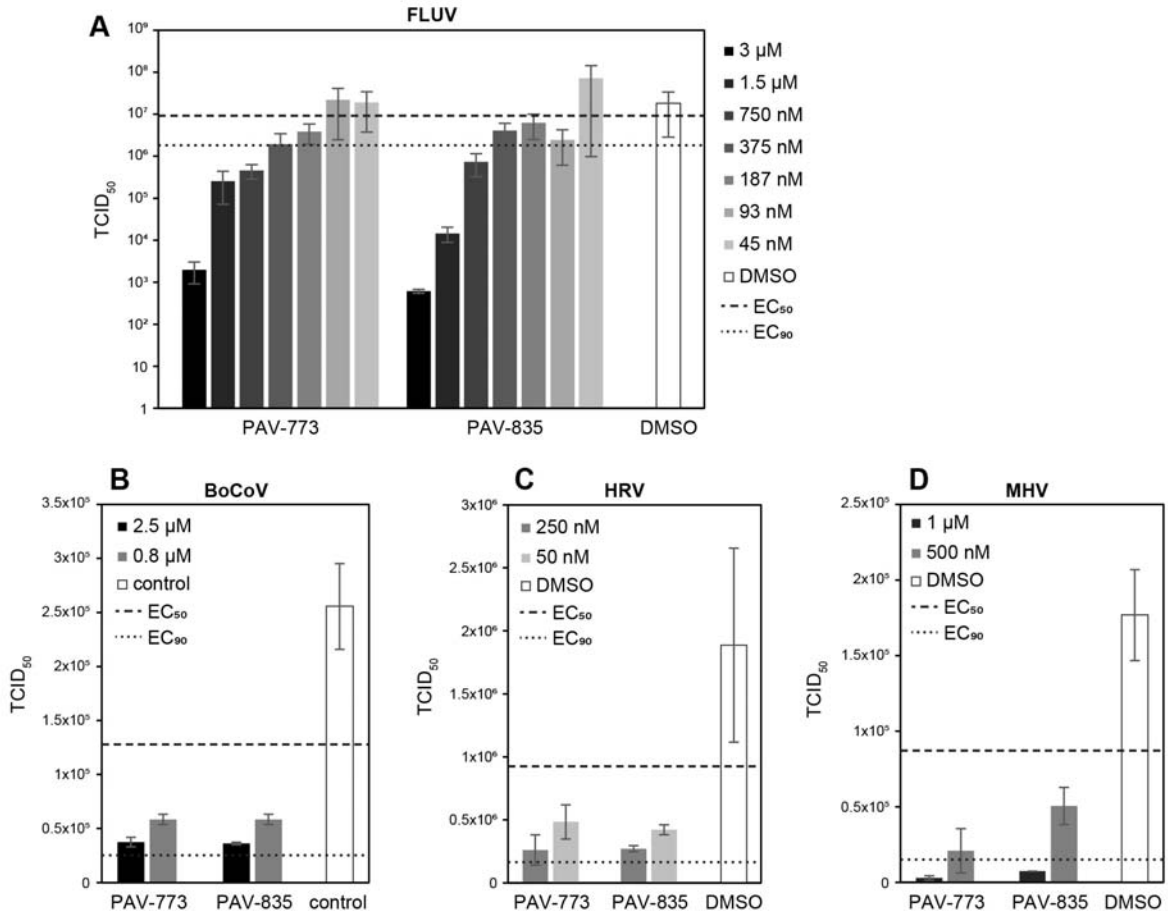

Legend to Figure 2. Assessment of pan-respiratory antiviral activity of early compounds PAV-773 and PAV-835, determined by $TCID_{50}$. Data shown are the averages of three biological replicates; error bars indicate standard error; DMSO is included as the vehicle control. (**A**) FLUV A/WSN/33 in MDCK cells. (**B**) BoCoV (BRCV-OK-0514-2) in HRT-18G cells, (**C**) HRV-16 in H1-HeLa cells, (**D**) MHV-68 in BHK-2 cells. Dashed line is the EC_{50}. Dotted line is the EC_{90}.

Assembly modulator compounds display a barrier to viral drug resistance development

Development of viral resistance has long been an Achilles heel of antiviral therapeutics (Nijhuis et al., 2009). Activity against FLUV provided the opportunity to compare early assembly modulators head to head with Oseltamivir, an antiviral small molecule targeting FLUV neuraminidase, which is known to select for viral resistance mutants (McKimm-Breschkin, 2013). Both PAV-835 and PAV-333 (a structurally unrelated assembly modulator chemotype), showed a significant barrier to development of resistance by FLUV (Table 1). The study was discontinued after the 7th passage, as the positive control Oseltamivir had substantially lost its antiviral activity.

		percent reduction in infection
Oseltamivir	passage 0 at 30 µM	91
	passage 7 at 30 µM	21.4
PAV-835	passage 0 at 3 µM	98.9
	passage 7 at 3 µM	91.9
PAV-333	passage 0 at 3 µM	94.5
	passage 7 at 3 µM	92.5

Legend to Table 1. Evidence for a barrier to resistance development. MDCK cells were infected with FLUV (A/WSN/33) in the presence of Oseltamivir (935 nM to 30 µM), PAV-835 (93.5 nM to 3 µM), or PAV-333 (93.5 nM to 3 µM). From passage to passage, drug concentrations were increased over the indicated ranges to encourage selection for resistance mutants. An initially Oseltamivir-sensitive FLUV strain became largely resistant after passage 7. In contrast, the two assembly modulator compounds PAV-835 and PAV-333 showed minimal loss of drug sensitivity.

Validation of early compounds in animals

Activity of a drug-like compound against such different viral families including viruses with RNA vs DNA genomes, and both enveloped and non-enveloped viruses, is unprecedented, so we sought early validation of its significance in animals. Compounds PAV-773 and PAV-835 were assessed in outbred pigs randomized within each litter into control and treatment groups and infected with porcine

epidemic diarrhea virus (PEDV), a coronavirus (Jung et al., 2020). Both compounds conferred a mortality benefit (Figure 3A). Notably, in the subset of litters in which all control animals died (i.e. severe disease), the treatment limb showed the same survival rate as that of the full treated population. Thus, efficacy of these compounds was not limited to mild disease—a property caveat for advancement of an antiviral drug for a disease with both mild and severe manifestations in different subpopulations, as is the case for SARS-CoV-2 (Gao et al., 2021). While the PEDV trial only assessed survival, a subsequent more advanced analog, PAV-431, was tested in cotton rats (Bem et al., 2011) infected with respiratory syncytial virus (RSV), a paramyxovirus, to assess viral titer (Figure 3C). A small but statistically significant drop in RSV titer was observed with drug treatment versus vehicle control. This indicated that the antiviral activity observed in cell culture would manifest in animals by both of the two metrics of interest: survival (including of a severe subset of an actual disease) and viral titer (in an animal model for a second viral family).

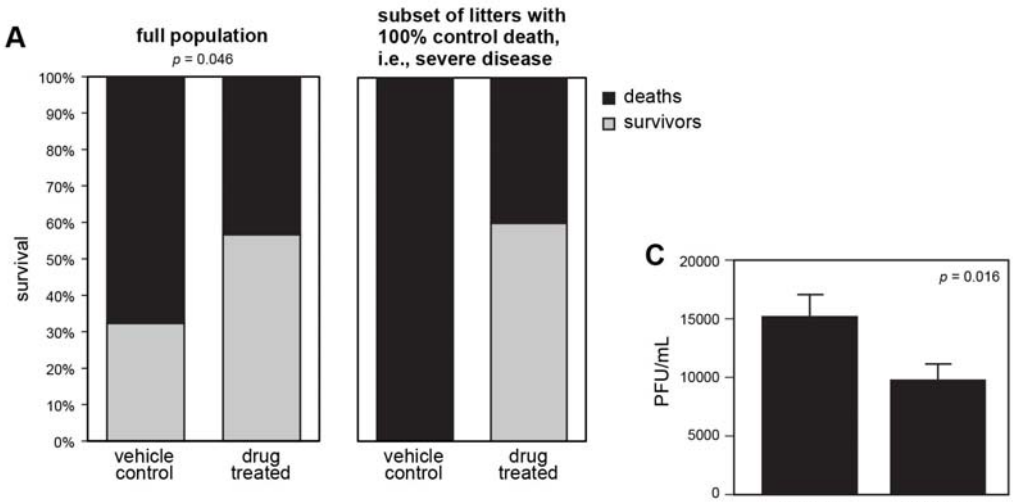

B

	control	PAV-835	PAV-773	control	PAV-835	PAV-773
% survival	32.3%	56.7%	56.7%	0.0%	57.1%	66.7%
survivors	10	17	17	0	8	10
deaths	21	13	13	15	7	5

Legend to Figure 3. Early analogs validated in animal efficacy trials. (**A-B**) PEDV pig trial, evaluated by survival. (**A**) Assembly modulator compounds demonstrated efficacy against both mild and severe disease. As PAV-773 and PAV-835 showed equal efficacy, they have been combined (Fisher exact test $p = 0.046$). The left panel shows percent survival for all animals in the study. The right panel shows the subset of litters in which all control animals (treated with vehicle only) died. (**B**) Breakdown of survival

for PAV-773 and PAV-835 separately for both the total population and the severe disease subset, where $p = 0.002$ and $p = 0.004$, respectively. This breakdown reveals the compounds to be as potent against mild disease (groups in which there were vehicle-only survivors) as in severe disease (groups in which there were no vehicle-only survivors). (**C**) RSV cotton rat trial, evaluated by day 5 lung viral titer determined by plaque assay. A significant drop in viral titer was observed with PAV-431 treatment (unpaired *t*-test $p = 0.016$). Data shown are averages; error bars indicate standard error.

Antiviral assessment against a wide range of respiratory viruses including SARS-CoV-2

Further studies with PAV-431 confirmed its activity against members of the six viral families causing > 95% of human respiratory disease (Figure 4A). Notably, PAV-431 shows no significant activity against rabies virus, suggesting specificity for a target present in a subset of viral families that includes the respiratory viruses. Upon onset of the COVID-19 pandemic, further studies in mammalian cells revealed activity of PAV-431 against multiple variants of SARS-CoV-2 (Figure 4B).

A

cell line	virus (family)	PAV-431 EC_{50}
MDCK	influenza A/WSN/33 (*Orthomyxoviridae*)	25 nM
MDCK	swine influenza virus SIV/SK WT (*Orthomyxoviridae*)	25 nM
GBK	bovine coronavirus (*Coronaviridae*)	50 nM
Vero E6	SARS-CoV-2 WA1/2020 (*Coronaviridae*)	100 nM
HEp2	respiratory synctial virus strain A-2 (*Paramyxoviridae*)	< 25 nM
HSAEC1-KT	Nipah virus rNiV-ZsG (*Paramyxoviridae*)	≤ 50 nM
A549	adenovirus serotype 5 strain adenoid 65 (*Adenoviridae*)	< 100 nM
H1-Hela	human cytomegalovirus strain AD69 (*Herpesviridae*)	25 nM
H1-Hela	human rhinovirus 16 (*Picornaviridae*)	< 20 nM
MNA	rabies virus CVS-11 (*Rhabdoviridae*)	> 400 nM

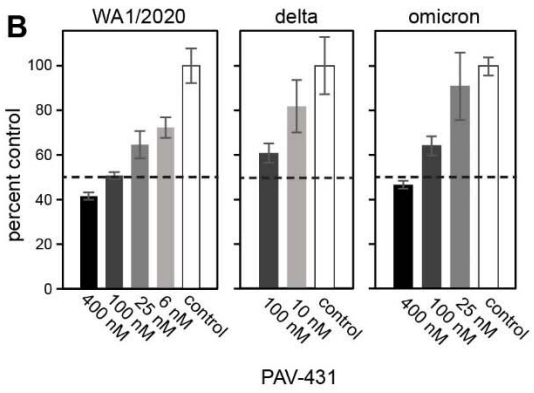

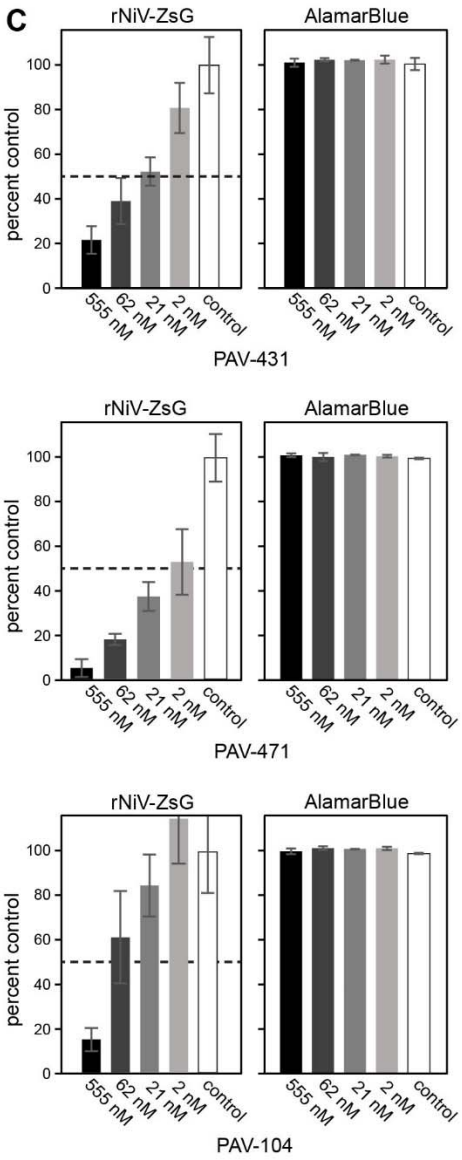

Legend to Figure 4. Pan-respiratory antiviral activity. (**A**) Efficacy of PAV-431 against each respiratory viral family in cell culture. **(B)** Dose-dependent antiviral activity of PAV-431against multiple SARS-CoV-2 strains: (WA1/2020, lineage A) in Vero E6 cells, determined by plaque assay, delta variant (lineage B.1.617.2) and omicron variant (lineage B.A.1) in Calu-3 cells determined by qPCR measurement of the SARS-CoV-2 E gene and/or $TCID_{50}$. Data shown are the averages of three biological replicates; error bars indicate standard error; DMSO is included as the vehicle control. **(C)**. Dose-dependent activity of PAV-431 and advanced analogs PAV-471 and PAV-104 against Nipah virus of the *Paramyxoviridae* family in primary-like human small airway epithelial cells (HSAEC1-KT)(Lo et al., 2014; Welch et al., 2020). Alamar Blue assessment of cytotoxicity shows no toxicity up to 5uM tested in 5mM glucose-supplemented minimum essential medium, so all therapeutic indices > 100.

Translation of antiviral treatments for human therapeutics presents a further challenge because animal models do not accurately reproduce human disease (Movia and Prina-Mello, 2020). It has been

proposed that the best predictor of human therapeutics is to take healthy human lung tissue from transplant donors, isolate primary bronchial epithelial cells, culture them to an air-liquid interface with differentiation to achieve polarity, tight junctions, motile cilia and mucus production, reproducing the relevant characteristics of the true target organ (Michi and Proud, 2021). The antiviral small molecule chemotype was assessed in this manner.

Efficacy in primary human airway epithelial cells at air-liquid interface

Primary human bronchial epithelial cells grown at an air-liquid interface represents the human airway with high fidelity including for studies of antiviral activity against SARS-CoV-2 (Fulcher and Randell, 2013; Ingber, 2020; Loo et al., 2020). In three of three lung donors whose bronchial epithelial cells were cultured to an air-liquid interface, infected with SARS-CoV-2, and treated with PAV-431, approximately 90% or more of viral load was eliminated compared to treatment with vehicle (Figure 5). Another more advanced analog, PAV-471 is also compared and shown to have significantly greater potency than PAV-431. It is notable that this *ex vivo* gold standard of translation to human therapeutics demonstrated even greater potency of both PAV-431 and PAV-471 than was observed in transformed cells.

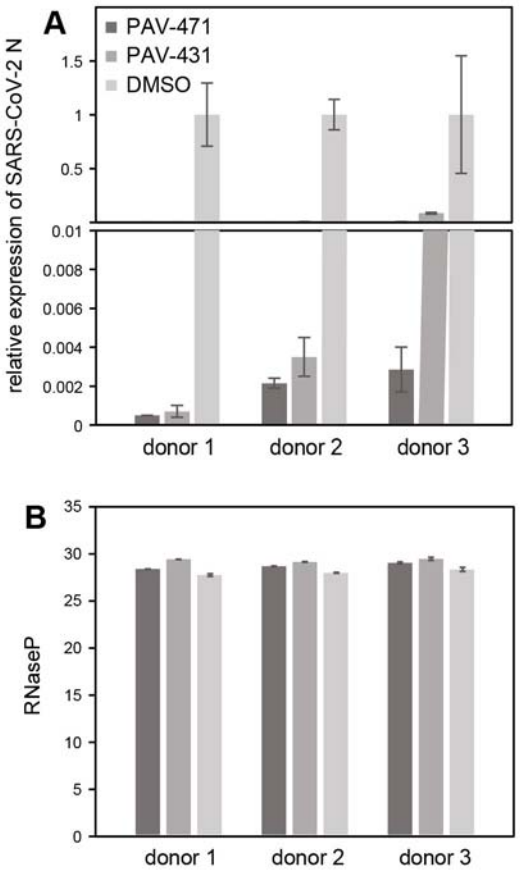

Legend to Figure 5. A. Assembly modulator compounds inhibit SARS-CoV-2 (gamma variant, lineage P.1) replication in primary human airway epithelial cells grown at an air-liquid interface, determined by qPCR measurement of the SARS-CoV-2 N gene. Data shown are the averages of two biological replicates; error bars indicate standard error; DMSO is included as the vehicle control. B. No significant toxicity was observed by assessment of levels of RNase P.

Drug target is a virally modified host multi-protein complex

Since the assembly modulators were discovered using a phenotypic CFPSA screen and were advanced based on structure-activity-relationship improvement of antiviral activity in mammalian cell culture, we as yet had no specific knowledge of the drug target. To identify the drug target, we developed a variation on the theme of drug resin affinity chromatography (DRAC) (Tanaka, 2009). PAV-431 was attached to a resin via a side group determined by structure-activity-relationship exploration to be non-essential for biological activity (Supplemental Figure S1 B). Cellular extracts were applied to drug resin columns to bind the target, washed, and then eluted with free drug compared to identical treatment of

control resin lacking the drug. These free drug eluates were found to contain a substantial set of proteins not observed with drug elution from the control resin. Early in the course of these studies, we discovered that conducting the procedure at temperatures between 22°C to 34°C rather than at 4°C, and supplementing with nucleotide triphosphates and an energy regenerating system, greatly enhanced target yield (Supplementary Figure S2). This distinctive energy-supplemented DRAC approach was given the acronym eDRAC.

*f*We used a PAV-431 drug resin to prepare eDRAC-free drug eluates which were then analyzed by tandem mass spectrometry (MS-MS) and by western blotting (WB) using commercial monospecific antibodies. Parallel MS-MS of eDRAC-free drug eluates from control resins lacking the drug affinity ligand demonstrated the high specificity of the set of proteins recovered from the drug resin, which notably included a number of known components of the host interactomes associated with respiratory viral lifecycles (Gordon et al., 2020b, 2020a; Perrin-Cocon et al., 2020; Watanabe et al., 2014) along with many members of host innate immune interactomes including that of autophagy (Mao et al., 2019; Zhao et al., 2021) (Figure 6A and Supplemental Figure S3). We compared eDRAC eluates from extracts of uninfected MRC-5 cells, BoCoV-infected or FLUV-infected MRC-5 cells, and infected MRC-5 cells treated with PAV-431 (Figure 6B-E). Infected cell eluates showed a striking enrichment of subsets of the proteins present, and substantial restoration upon drug treatment to that observed from uninfected cells, even more so for BoCoV infection than for FLUV infection (Supplementary Figure S3).

To provide independent corroboration of the conclusions from these eDRAC MS-MS studies, PAV-431 analogs were synthesized in which a biotin and a diazirine UV photocross-linking moiety were attached at the same position to which the compound had been attached to the resin for eDRAC analysis (Supplementary Figure S1C). After UV crosslinking to the protein nearest the assembly modulator, streptavidin precipitation isolated the relevant multi-protein complex (co-precipitated under non-denaturing conditions). A number of the proteins identified by MS-MS and/or Western blot in eDRAC free drug eluates were confirmed in this way to be part of a multi-protein complex, including p62/SQSTM1, VCP/p97, and CAPN2 (Figure 6G).

Identification of the drug-binding protein within the target multi-protein complex

If, subsequent to UV light exposure, the sample was denatured and then subjected to streptavidin precipitation, only the nearest neighbor protein(s) covalently bound to the drug-biotin conjugate will be found in the streptavidin precipitate. One protein, 14-3-3, a member of the 14-3-3 family of allosteric modulators implicated in the pathophysiology of many different respiratory viral families (Gupta et al., 2020; Jia et al., 2017; Liu et al., 2021; Obsilova and Obsil, 2020; Pei et al., 2011; Stevers et al., 2018; Tugaeva et al., 2021) was present on streptavidin precipitation of samples prepared by both native and denaturing conditions, identifying 14-3-3 as the direct drug-binding protein.

A notable observation was that the fraction of each of these proteins, including 14-3-3, found in the target complex was extremely small (< 5%) compared to the total amount of that protein present in the starting cellular extract (Figure 6G). The fidelity of this surprising observation was confirmed by rerun of extract eDRAC flow through onto a second eDRAC column demonstrating complete depletion of the target with no further binding to the second eDRAC column (Supplementary Figure S4). The flow through from the control column, from which the target had not been depleted, when analyzed on a second eDRAC column, consistently revealed that the small fraction of the set of target proteins could still be bound and eluted with free drug (Supplementary Figure S4). Thus, the small amount of 14-3-3 and other proteins identified in the target multi-protein complex from the initial eDRAC column are unique in their biochemical behavior, comprising a distinctive subset present in the form of the identified target multi-protein complex, and distinct from the > 95% of the individual protein components that do not bind the drug resin, even under eDRAC conditions. The implications of this important finding are discussed below.

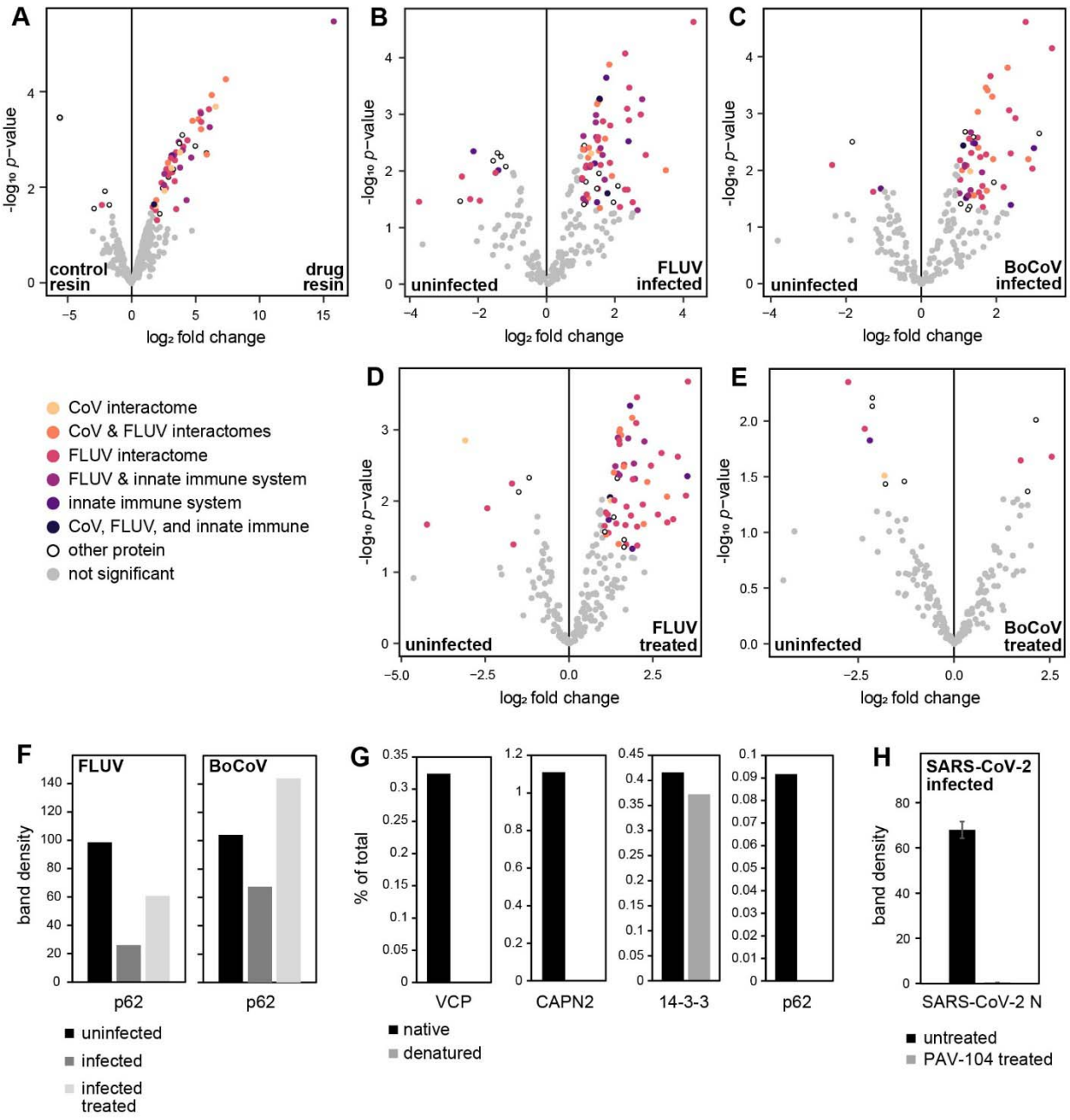

Legend to Figure 6. Drug target is a host multi-protein complex modified by viral infection and restored with drug treatment. (**A-E**) Volcano plots visualizing the protein composition of the target complex determined by MS-MS on triplicate eDRAC eluates from extracts of MRC-5 cells that were either uninfected, infected with FLUV or BoCoV, or infected and treated with PAV-431. Significant proteins ($|\log_2$ fold change$| > 1$ and p-value < 0.05) are colored based on their known involvement in the CoV, FLUV, and innate immune system interactomes and listed in Supplementary Figure S3. (**A**) Comparison between control resin and PAV-431 drug resin demonstrates drug specificity of the target complex. (**B-C**) Infection with FLUV (B) or BoCoV (C) modifies the target complex. (**D-E**)**,** Treatment with PAV-431 restores the target to the uninfected state, partially for FLUV (D) and almost completely for BoCoV (E). (**F**) eDRAC eluates from MRC-5 cells (left) and HRT-18G cells (right), uninfected or infected with either

FLUV (left) or BoCoV (right), analyzed by SDS-PAGE and WB for target component p62. In both cases, viral infection resulted in a diminution of p62, which was restored by treatment with PAV-431 (right) and PAV-818 (left). (**G**) Crosslinked eDRAC eluates from pig lung extract co-precipitated under native or denaturing conditions and analyzed by SDS-PAGE and WB for target components p62, VCP, CAPN2, and 14-3-3. Presence under both conditions identifies 14-3-3 as the direct drug binding protein, while loss under denaturing conditions identifies the others as more distal components of the complex associated with the drug indirectly via other proteins in the complex that are associated with the direct-binding protein 14-3-3. (**H)** SARS-CoV-2 infected an PAV-431-treated cell lysate subjected to PAV-431 photocross-linking and streptavidin precipitation under non-denaturing conditions. A-E and H show the statistical significance of the findings, F and G show representative individual experiments. Drug concentration for treatment of infected cells in H was 100nM.

Target Product Profile

Given the striking pan-respiratory antiviral activity shown, we chose to more fully assess the target product profile of PAV-431, that is, to determine its drug-like properties by the standard criteria for advancement of a drug candidate (Breder et al., 2017). PAV-431 displayed promising properties including being negative for hERG channel inhibition, negative for mutagenicity by the Ames test, negative for significant cytochrome P-450 inhibition, and without substantial Cerep panel enzyme inhibition liabilities (Supplementary Figure S5). PAV-431 itself was disqualified from further consideration for human pan-respiratory therapeutics due to an insufficient safety profile in rodents (Supplementary Figure S6). Nevertheless, these studies demonstrated that this chemotype has reasonable drug-like properties and lacks various other liabilities. Molecular properties relating to Lipinski's rule of five are presented in Supplementary Table S1. Going forward, lead series advancement efforts focused on eliminating host toxicity.

Lead series advancement lowers host toxicity while maintaining pan-respiratory viral family antiviral activity

Additional analogs were synthesized and screened for antiviral activity and host toxicity as assessed by maximal tolerated dose (MTD) in mice. Two analogs in particular were notable in comparison to PAV-431. PAV-471 was substantially more active, including in human bronchial epithelial cells cultured to an air-liquid interface (Figure 5), but also more toxic in mice (Supplementary Figure S6).

PAV-104 however, was both more active and less toxic than PAV-431, with improved pharmacokinetic properties making it suitable for once daily dosing orally, compared to PAV-431 (Figure 7). The non-toxicity of PAV-104 was confirmed by numerous criteria. These included maximum tolerated dose with no observable effect level of 15 mg/kg or mild toxicity of 20mg/kg by intraperitoneal route in mice, and no observable adverse effects at < 75 mg/kg by and only mild toxicity at > 250mg/kg by oral route in rats (Figure 7A); acute repeat dose toxicology in rats with a 50mg/kg oral dose daily for 7 days showed no toxic signs of any sort, including behavioral, clinical chemistry, hematology, or gross pathology assessment. Trough plasma levels on the 7^{th} day exceeded EC_{50} by >100x (Figure 7B). Pharmacokinetic studies in rats demonstrated further properties desired for a clinical candidate including good oral bioavailability (32%), half-life (9 hours), and lung exposure (2.4x plasma level at 24 hours) (Figure 7A).

331

A

		PAV-773			PAV-835		PAV-431			PAV-471		PAV-104		
mouse maximum tolerated dose	safe dose route-dosage (mg/kg)	-	IP-5	-	-	IP-1	-	IP-5	-	-	IP-1	-	IP-15	PO-50
	toxic dose route-dosage (mg/kg)	-	IP-15	-	-	IP-15	-	IP-10	-	-	IP-2	-	IP-20	PO-250
repeat dose toxicology [a] mouse 10 day [b] rat 7 day	route-dosage (mg/kg)	-	IP-5[a]	-	-	IP-1[a]	-	IP-2[a]	-	-	-	-	-	PO-50[b]
	body weight, clinical signs, histopathology, clinical parameters	-	NAD/ NSSD	-	-	NAD/ NSSD	-	NAD/ NSSD	-	-	-	-	-	NAD/ NSSD
rat PK [c] mouse	route-dosage (mg/kg)	IV-1[c]	IP-5[c]	PO-5[c]	IV-0.2	IP-1	IV-1	IP-5	PO-5	IV-0.2	IP-1	IV-1	IP-5	PO-20
	AUC_{last} (nM.h)	2287	733	253	428	1043	831	2464	low conc.	108	371	543	2510	3247
	AUC_{inf} (nM.h)	ND	ND	ND	428	1047	926	2499		135	387	559	2656	3620
	C_{max} (nM)	ND	1035	51	1608	2842	685	793		152	550	1379	2243	1417
	T_{max} (h)	ND	0.08	4	0.03	0.08	0.08	0.25		0.08	0.25	0.08	0.25	0.5
	$t_{½}$ (h)	ND	ND	ND	0.5	0.4	12	5		4	2	2	7	9
	CL (mL/min)	1.3	-	-	25	-	49	-		45	-	51	-	-
	V_z (L/Kg)	13.3	-	-	0.5	-	32	-		12	-	4	-	-
	F (%)	-	7	2.2	-	49	-	59		-	69	-	95	32
rat uptake [c] mouse timepoints: [d] 5 min [e] 30 min [f] 1 hour [g] 2 hours [h] 24 hours	route-dosage (mg/kg)	-	IP-5[c]	-	-	IP-1[c]	-	IP-5	-		IP-1	-	IP-5	PO-20
	concentration in lungs (nM)	-	866[d] 109[f]	-	-	98[e] 5[g]	-	1224[e] 355[g]	-	-	739[e] 175[g]	-	160[e] 485[g]	306[e] 113[g] 53[h]
	concentration in brain (nM)	-	2148[d] 169[f]	-	-	178[e] 20[g]	-	1416[e] 479[g]	-	-	334[e] 69[g]	-	17[e] BLOQ[g]	26[e] BLOQ[g] BLOQ[h]
	concentration in plasma (nM)	-	1657[d] 250[f]	-	-	181[e] 18[g]	-	834[e] 333[g]	-	-	265[e] 40[g]	-	397[e] 261[g]	1011[e] 371[g] 22[h]

B

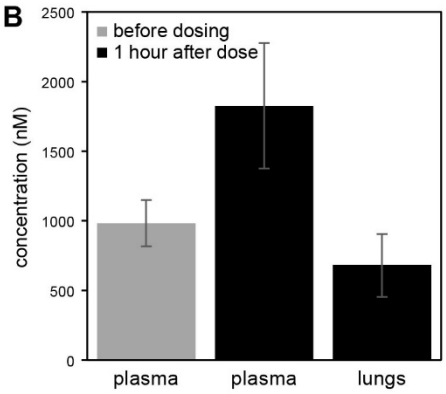

332
333

334 **Legend to Figure 7.** Pharmacokinetic and toxicological assessment of the lead series in BALB/c mice
335 and Sprague Dawley rats. (**A**) Summary of results. IV, intravenous; IP, intraperitoneal; PO, per oral; PK,
336 pharmacokinetics; AUC_{last}, area under the curve from time zero to the last quantifiable concentration;
337 AUC_{inf}, area under the curve vs. time curve extrapolated to infinity; C_{max}, peak plasma concentration;
338 T_{max}, time of peak concentration observed; $t_{1/2}$, terminal half-life; CL, steady-state clearance; V_z, volume
339 of distribution; F, fraction bioavailability; NAD, no abnormality detected; NSSD, no significant statistical
340 difference; BLOQ, below level of quantification; ND, not determined. Pharmacokinetic parameters were
341 determined using WinNonlin software. **(B)** PAV-104 levels following acute repeat dose toxicology
342 evaluation in Sprague Dawley rats with a daily oral dose of 50 mg/kg for 7 days. Trough plasma levels
343 exceed EC_{50} by ~100 fold. Data shown are the averages of 5 animals; error bars indicate standard
344 deviation.

A body of literature has implicated 14-3-3 proteins, known to be allosteric modulators (Obsilova and Obsil, 2020), as interacting with SARS-CoV-2 N protein (Tugaeva et al., 2021). Based on those studies we predicted that PAV-104, while directly crosslinked to 14-3-3 in a complex containing other proteins including CAPN2 and VCP, should be indirectly associated with SARS-CoV-2 N protein by virtue of transient protein-protein interactions in the host multi-protein complex drug target, during capsid assembly. This was confirmed with extracts of Calu-3 cells infected with SARS-CoV-2 vs infected and treated with PAV-104 at 100nM. As predicted, SARS-CoV-2 N co-precipitated with streptavidin under native conditions and was substantially diminished after 24 hrs of treatment with PAV-104 (Figure 6H).

Finally, to confirm the principle of pan-respiratory anti-viral activity for PAV-104, primary-like human small airway epithelial cells were infected with Nipah virus, a BSL-4 virus belonging to the *Paramyxoviridae* family designated by the WHO as a priority pathogen pandemic potential ("WORKSHOP ON PRIORITIZATION OF PATHOGENS," 2015; "WHO publishes list of top emerging diseases likely to cause major epidemics," 2015). Figure 4C demonstrates activity of PAV-431, PAV-471 and PAV-104 against Nipah virus. The advanced analog PAV-104 with a strikingly improved safety profile, has maintained the pan-viral family activity for diverse respiratory viral families as observed for the earlier analogs PAV-773, PAV-835 and PAV-431.

Discussion

This antiviral chemotype, several of whose lead series compounds are studied here, exhibits remarkable features. These include activity across a broad range of respiratory viral families and a barrier to development of viral drug resistance. The antiviral activity was demonstrated both in cell culture and in animals. Cell culture studies, including in primary human bronchial epithelial cells cultured at an air-liquid interface and infected with SARS-CoV-2, confirmed the antiviral potency demonstrated in various cell lines, with members of six major respiratory viral families, by a variety of assay methods (Figures 2,4,5). Animal studies, carried out on early analogs in the lead series, validated efficacy for survival in an

actual pig coronavirus disease (Figure 3A), and by viral load reduction in the cotton rat model of RSV infection (Figure 3B). A barrier to resistance development was demonstrated for an early analog on influenza compared to oseltamivir, which targets a viral gene product, and to which resistance rapidly developed (Table 1). It should be noted that structurally unrelated host-targeted assembly modulators potent against HIV have maintained a barrier to resistance development for the full 37 cycles of selection attempted (Reed et al., 2021). These findings suggest that the barrier to resistance development posed by host-targeted assembly modulators as a general therapeutic class may be substantial. Subsequently, through structure-activity relationship advancement, antiviral activity in cell culture against SARS-CoV-2 has been increased >10x with the advent of analogs PAV-471 and PAV-104, the latter of which also displays pharmacokinetic properties and safety in rats worthy of continued advancement to investigational new drug (IND) enabling studies towards human therapeutics.

Target identification by DRAC revealed a previously undescribed multi-protein complex whose constituents include proteins implicated in diverse respiratory viral lifecycles. A number of the multi-protein complex constituent proteins are part of innate immune interactomes, including autophagy, all important for host antiviral defense (Deretic, 2021). Upon viral infection the composition of the target host multi-protein complex is shown to change, with increase in specific members of both the viral lifecycle and innate immune subsets of component proteins (Figure 6). One protein in particular, p62/SQSTM1, a key regulator of autophagy, is lost upon viral infection by both CoV and FLUV. This is consistent with the hypothesis that the virus has used deep evolutionary time and natural selection to identify a host allosteric site that allows it to both repurpose critical host machinery to viral replication and block autophagic host defenses. This chemotype appears to substantially reverse the virally induced changes of composition of the target host multi-protein complex for each of the different respiratory viral families studied.

Figure 8 summarizes our current working hypothesis for the dual modes of action of these drugs, including PAV-431 and PAV-104, namely, targeting an allosteric site important for both viral replication/blockade and decoupling/restoration of p62/SQSTM1, a mediator of host autophagic innate

immune defenses. That the drugs block viral replication is supported by the demonstrated drop in viral load by both plaque assay and $TCID_{50}$ in cell culture (Figure 4A). The interaction with the SARS-CoV-2 N protein and its diminution upon drug treatment (Figure 6H) provides a structural basis for this functional observation, consistent with recent literature implicating transient interactions as druggable targets (Kii et al., 2016; Umezawa and Kii, 2021). The hypothesized restoration of autophagy by drug treatment is supported by the demonstration that p62/SQSTM1 is present in the target complex in uninfected cells, is lost from the complex upon viral infection, and is largely restored after 24hrs of drug treatment (Figure 6F).

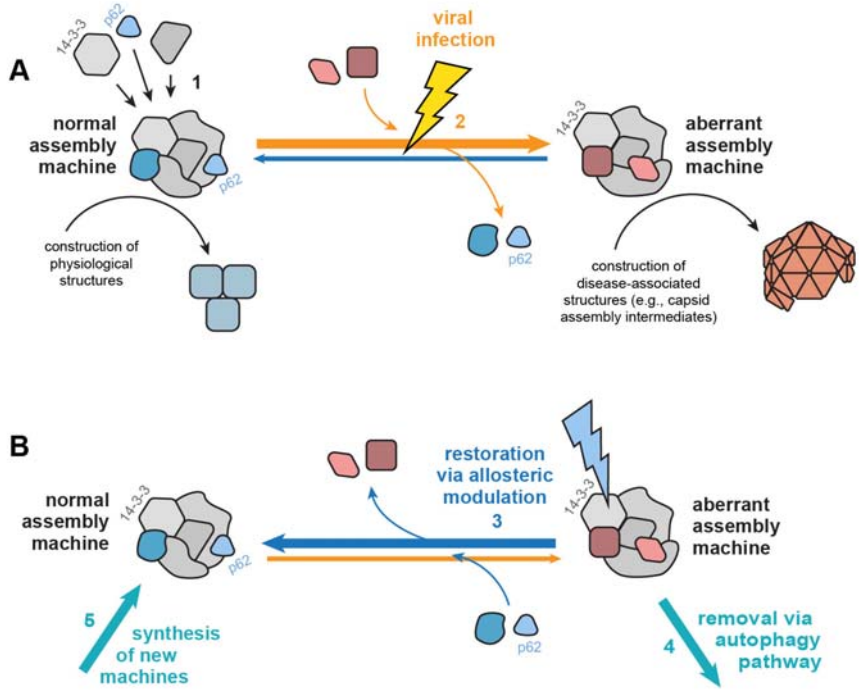

Figure 8. Cartoon summarizing our working hypothesis on assembly modulation therapeutics. (**A**) Normal assembly machines are transient host multi-protein complexes that come together to carry out various events involved in the construction of physiological structures and maintenance of homeostasis (1). Viruses have evolved to co-opt the assembly machines of their hosts to meet their own needs, presumably through signaling pathway manipulation and/or allosteric site modulation (2). This results in the formation of aberrant assembly machines that do something they are not supposed to do (e.g. build a viral capsid) and perhaps fails to do something they are supposed to do (e.g. inform innate immunity that the cell is under viral attack) due to loss of autophagy regulator p62. The former action is reflected as viral replication and the latter action is reflected in the failure of autophagic innate immune defense. Both consequences manifest as disease and their molecular basis is the normal to aberrant change in assembly machine composition. (**B**) Treatment with assembly modulators results in elimination of aberrant

assembly machines and restoration of normal assembly machines. This could be a result of either direct action on the allosteric site (e.g. affecting protein-protein interactions such that the normal assembly machine is stabilized) or indirectly by activation of autophagy to destroy the aberrant assembly machines (4) followed by homeostatic feedback repopulation of normal assembly machines (5).

Of the plethora of proteins found in the eDRAC eluate and photocross-link streptavidin precipitate, only 14-3-3 was found to be a direct drug-binding protein. 14-3-3 proteins have been implicated both as allosteric modulators of protein kinases (Obsilova and Obsil, 2020) and in direct interaction with SARS-CoV-2 N (Tugaeva et al., 2021), consistent with our findings. These changes in target multi-protein complex composition suggest that upon viral infection the multi-protein complex is repurposed from the role of a normal assembly machine performing transient functions that maintain host homeostasis, to an aberrant assembly machine that is involved in viral capsid assembly and is disconnected from host antiviral defense mechanisms such as autophagy. Upon assembly modulator drug treatment, both these features of infection are reversed, albeit more so for CoV infection than for FLUV infection at the 24h time point assessed. Whether that difference reflects a distinction intrinsic to those two viral families (*Coronaviridae* vs *Orthomyxoviridae*) or is simply a consequence of a different time course of viral-host interaction and reversal for these two viral families, remains to be determined. The present methods applied to study of multiple members of each viral family, and at other time points in the course of infection and drug treatment, should be able to clarify this issue. Regardless, the notion that one target can reverse both types of changes for multiple viral families is notable and likely contributes to the potency of this antiviral mechanism.

Why has this remarkable host targeted pan-respiratory antiviral mechanism been overlooked previously? The data presented suggest at least two reasons, both related to the unusual nature of the drug target. First, because the target is both transient and energy-dependent – not just for its action, but also for its formation. These features make it extremely difficult to detect by conventional proteomics (Aslam et al., 2017), limitations that were overcome by use of the CFPSA phenotypic screen to find the chemotype, and the eDRAC/photo cross-linking protocols used to characterize its target.

A second feature that made this antiviral mechanism hard to detect is the small percent of the total of each of the proteins that are present in the host multi-protein complex target, even with eDRAC enhancement. The burgeoning literature on "moonlighting" functions of innumerable proteins (Alpert et al., 2021; Bhutta et al., 2021; Copley, 2012; Jeffery, 2019) suggests that there are subsets of proteins, identical in amino acid sequence, performing different functions within cells. Whether such differences in function are due to differences in post-translational covalent modification (Liu et al., 2016; Song and Luo, 2019; Xu et al., 2019), intrinsically unfolded domains that are templated by the other proteins with which the subset is associated (Uversky, 2016), or due to some other mechanism such as different pathways of biogenesis (Alpert et al., 2021; Lingappa et al., 2002; Williams and Dichtl, 2018) remains to be determined and likely will vary on a case-by-case basis.

Despite the ample evidence for protein functional heterogeneity in living cells as cited above, molecular genetic manipulation of coding sequences and recombinantly expressed protein remains the primary, and often exclusive, bases for most protein structural studies including of drug targets. The present data builds on the power of genetic studies, but calls exclusive use of that approach into question, not just for drug discovery, but also with regards to an understanding of biological regulation. This is because functionally distinct subsets of individual proteins, assembled co-translationally (Williams and Dichtl, 2018), perhaps in a contingent manner (Lingappa et al., 2002), are unlikely to be parsed by upstream genomic and transcriptomic analyses. New tools, such as the eDRAC and photocross-linking drug analog protocols used here, may facilitate the difficult but essential task of studying protein heterogeneity as expressed physiologically in cells and tissues. Other methods, including non-invasive chemical modification (Alpert et al., 2021) and conformation-specific monoclonal antibodies (Akuta et al., 2022; Leliveld and Korth, 2007), may also be valuable for this effort. This critique applies not just to exclusive use of methods such as siRNA knockdown and CRISPR that manipulate gene expression before protein biogenesis and assembly has occurred, but more generally to the use of recombinantly expressed protein as the substrate for structural and functional studies.

Perhaps the most remarkable of our findings is that members of such diverse viral families should have their replication effectively blocked by a single host-targeted small molecule. On the one hand, this implies a shared drug-binding protein. Most likely that shared drug target, a distinctive subset of the protein 14-3-3, is found in each of the different aberrant assembly machines generated by each of these diverse viral families from a common host multi-protein complex. We hypothesize that utilization of this single shared host multi-protein complex is a consequence of virus-host co-evolution. On the other hand, the data in Figure 6 suggests that different viral families can modify the same host multi-protein complex in which the direct drug target 14-3-3 is a component, in different ways. While this could be accounted for by various explanations, perhaps the most straightforward is as a manifestation of allostery (Fenton, 2008; Motlagh and Hilser, 2012), given that the direct drug-binding protein, 14-3-3, is a known allosteric modulator (Obsilova and Obsil, 2020). The drugs described here could work by stabilization of the normal assembly machine, perhaps with re-activation of autophagy upon restoration of p62/SQSTM1 to the host multi-protein complex, thereby serving to eliminate aberrant assembly machines. Alternatively, direct binding of the drug to the allosteric site within the aberrant assembly machine could mediate in real time the change in equilibrium described in Figure 8. These and other models remain to be explored, which the methods described here should facilitate.

Upper respiratory tract infection is generally accepted to progress to lower respiratory tract disease in the subset of patients who become seriously ill from respiratory viruses (Florin et al., 2017). Furthermore respiratory antiviral efficacy is crucially dependent on early treatment (Fry et al., 2014; Muthuri et al., 2014; Waghmare et al., 2019). Due to the diversity of viral families that cause respiratory viral disease, utility of previous antiviral compounds (e.g. Oseltamivir) requires rapid identity of the causative virus, as efficacy is limited to a particular viral family. Typically, by that time, infection has largely resolved or has progressed to the lower respiratory tract in the case of severe disease and with its variable attendant complications (e.g. cytokine storm). However, a non-toxic compound active against all of the major respiratory viral families—be they RNA or DNA viruses, enveloped or not—would make it possible to initiate treatment early, at the onset of upper respiratory tract viral symptoms, in order to

prevent progression to the lower respiratory tract, and thereby achieve optimal benefit in shortening the duration and severity of illness. Thus, the compounds presented here may have transformative implications for the treatment of respiratory viral disease, applicable to everything from seasonal FLUV, common "winter viruses" (RSV, HRV, etc.), to SARS-CoV-2, and other emerging viruses, as well as the common cold. This could be of particular importance for people at risk, whether because of age, comorbidities, immunosuppression, or airway hyper-reactivity (e.g. asthma/COPD), and for periods of widespread infection by highly pathogenic viruses.

References

Akuta, T., Maruyama, T., Sakuma, C., Nakagawa, M., Tomioka, Y., Entzminger, K., Fleming, J.K., Sato, R., Shibata, T., Kurosawa, Y., Okumura, C.J., Arakawa, T., 2022. A New Method to Characterize Conformation-Specific Antibody by a Combination of Agarose Native Gel Electrophoresis and Contact Blotting. Antibodies Basel Switz. 11, 36. https://doi.org/10.3390/antib11020036

Alpert, E., Akhavan, A., Gruzman, A., Hansen, W.J., Lehrer-Graiwer, J., Hall, S.C., Johansen, E., McAllister, S., Gulati, M., Lin, M.-F., Lingappa, V.R., 2021. Multifunctionality of Prostatic Acid Phosphatase in Prostate Cancer Pathogenesis. Biosci. Rep. BSR20211646. https://doi.org/10.1042/BCJ20200944

Andrei, S.A., Sijbesma, E., Hann, M., Davis, J., O'Mahony, G., Perry, M.W.D., Karawajczyk, A., Eickhoff, J., Brunsveld, L., Doveston, R.G., Milroy, L.-G., Ottmann, C., 2017. Stabilization of protein-protein interactions in drug discovery. Expert Opin. Drug Discov. 12, 925–940. https://doi.org/10.1080/17460441.2017.1346608

Aslam, B., Basit, M., Nisar, M.A., Khurshid, M., Rasool, M.H., 2017. Proteomics: Technologies and Their Applications. J. Chromatogr. Sci. 55, 182–196. https://doi.org/10.1093/chromsci/bmw167

Bem, R.A., Domachowske, J.B., Rosenberg, H.F., 2011. Animal models of human respiratory syncytial virus disease. Am. J. Physiol. Lung Cell. Mol. Physiol. 301, L148-156. https://doi.org/10.1152/ajplung.00065.2011

Bhutta, M.S., Gallo, E.S., Borenstein, R., 2021. Multifaceted Role of AMPK in Viral Infections. Cells 10, 1118. https://doi.org/10.3390/cells10051118

Blobel, G., 2000. Protein targeting (Nobel lecture). Chembiochem Eur. J. Chem. Biol. 1, 86–102. https://doi.org/10.1002/1439-7633(20000818)1:2<86::AID-CBIC86>3.0.CO;2-A

Blueprint for R&D preparedness and response to public health emergencies due to highly infectious pathogens [WWW Document], 2015.

Breder, C.D., Du, W., Tyndall, A., 2017. What's the Regulatory Value of a Target Product Profile? Trends Biotechnol. 35, 576–579. https://doi.org/10.1016/j.tibtech.2017.02.011

Broce, S., Hensley, L., Sato, T., Lehrer-Graiwer, J., Essrich, C., Edwards, K.J., Pajda, J., Davis, C.J., Bhadresh, R., Hurt, C.R., Freeman, B., Lingappa, V.R., Kelleher, C.A., Karpuj, M.V., 2016. Biochemical and biophysical characterization of cell-free synthesized Rift Valley fever virus nucleoprotein capsids enables in vitro screening to identify novel antivirals. Biol. Direct 11, 25. https://doi.org/10.1186/s13062-016-0126-5

Copeland, K., Hansen, W., Asundi, V., Hong, S., Chamberlin, J., Dey, D., Broce, S., Himmel, H., Decloutte, C., Ram, S., Steffen, I., Pöhlmann, S., Lingappa, J.R., Hurt, C.R., Lingappa, V.R.,

2010. Protein–Protein Interactions Occurring During HIV Capsid Assembly in a Cell-free Protein Synthesizing System. Antiviral Res. 86, A22. https://doi.org/10.1016/j.antiviral.2010.02.339

Copley, S.D., 2012. Moonlighting is mainstream: paradigm adjustment required. BioEssays News Rev. Mol. Cell. Dev. Biol. 34, 578–588. https://doi.org/10.1002/bies.201100191

Deretic, V., 2021. Autophagy in inflammation, infection, and immunometabolism. Immunity 54, 437–453. https://doi.org/10.1016/j.immuni.2021.01.018

European Food Safety Authority, European Centre for Disease Prevention, Control, European Union Reference Laboratory for Avian Influenza, Adlhoch, C., Fusaro, A., Gonzales, J.L., Kuiken, T., Marangon, S., Niqueux, É., Staubach, C., Terregino, C., Aznar, I., Muñoz Guajardo, I., Baldinelli, F., 2021. Avian influenza overview September - December 2021. EFSA J. Eur. Food Saf. Auth. 19, e07108. https://doi.org/10.2903/j.efsa.2021.7108

Fenton, A.W., 2008. Allostery: an illustrated definition for the 'second secret of life.' Trends Biochem. Sci. 33, 420–425. https://doi.org/10.1016/j.tibs.2008.05.009

Florin, T.A., Plint, A.C., Zorc, J.J., 2017. Viral bronchiolitis. Lancet Lond. Engl. 389, 211–224. https://doi.org/10.1016/S0140-6736(16)30951-5

Fry, A.M., Goswami, D., Nahar, K., Sharmin, A.T., Rahman, M., Gubareva, L., Azim, T., Bresee, J., Luby, S.P., Brooks, W.A., 2014. Efficacy of oseltamivir treatment started within 5 days of symptom onset to reduce influenza illness duration and virus shedding in an urban setting in Bangladesh: a randomised placebo-controlled trial. Lancet Infect. Dis. 14, 109–118. https://doi.org/10.1016/S1473-3099(13)70267-6

Fulcher, M.L., Randell, S.H., 2013. Human nasal and tracheo-bronchial respiratory epithelial cell culture. Methods Mol. Biol. Clifton NJ 945, 109–121. https://doi.org/10.1007/978-1-62703-125-7_8

Gao, Y.-D., Ding, M., Dong, X., Zhang, J.-J., Kursat Azkur, A., Azkur, D., Gan, H., Sun, Y.-L., Fu, W., Li, W., Liang, H.-L., Cao, Y.-Y., Yan, Q., Cao, C., Gao, H.-Y., Brüggen, M.-C., van de Veen, W., Sokolowska, M., Akdis, M., Akdis, C.A., 2021. Risk factors for severe and critically ill COVID-19 patients: A review. Allergy 76, 428–455. https://doi.org/10.1111/all.14657

Goodacre, N., Devkota, P., Bae, E., Wuchty, S., Uetz, P., 2020. Protein-protein interactions of human viruses. Semin. Cell Dev. Biol. 99, 31–39. https://doi.org/10.1016/j.semcdb.2018.07.018

Goodwin, C.M., Xu, S., Munger, J., 2015. Stealing the Keys to the Kitchen: Viral Manipulation of the Host Cell Metabolic Network. Trends Microbiol. 23, 789–798. https://doi.org/10.1016/j.tim.2015.08.007

Gordon, D.E., Hiatt, J., Bouhaddou, M., Rezelj, V.V., Ulferts, S., Braberg, H., Jureka, A.S., Obernier, K., Guo, J.Z., Batra, J., Kaake, R.M., Weckstein, A.R., Owens, T.W., Gupta, M., Pourmal, S., Titus, E.W., Cakir, M., Soucheray, M., McGregor, M., Cakir, Z., Jang, G., O'Meara, M.J., Tummino, T.A., Zhang, Z., Foussard, H., Rojc, A., Zhou, Y., Kuchenov, D., Hüttenhain, R., Xu, J., Eckhardt, M., Swaney, D.L., Fabius, J.M., Ummadi, M., Tutuncuoglu, B., Rathore, U., Modak, M., Haas, P., Haas, K.M., Naing, Z.Z.C., Pulido, E.H., Shi, Y., Barrio-Hernandez, I., Memon, D., Petsalaki, E., Dunham, A., Marrero, M.C., Burke, D., Koh, C., Vallet, T., Silvas, J.A., Azumaya, C.M., Billesbølle, C., Brilot, A.F., Campbell, M.G., Diallo, A., Dickinson, M.S., Diwanji, D., Herrera, N., Hoppe, N., Kratochvil, H.T., Liu, Y., Merz, G.E., Moritz, M., Nguyen, H.C., Nowotny, C., Puchades, C., Rizo, A.N., Schulze-Gahmen, U., Smith, A.M., Sun, M., Young, I.D., Zhao, J., Asarnow, D., Biel, J., Bowen, A., Braxton, J.R., Chen, J., Chio, C.M., Chio, U.S., Deshpande, I., Doan, L., Faust, B., Flores, S., Jin, M., Kim, K., Lam, V.L., Li, F., Li, J., Li, Y.-L., Li, Y., Liu, X., Lo, M., Lopez, K.E., Melo, A.A., Moss, F.R., Nguyen, P., Paulino, J., Pawar, K.I., Peters, J.K., Pospiech, T.H., Safari, M., Sangwan, S., Schaefer, K., Thomas, P.V., Thwin, A.C., Trenker, R., Tse, E., Tsui, T.K.M., Wang, F., Whitis, N., Yu, Z., Zhang, K., Zhang, Y., Zhou, F., Saltzberg, D., QCRG Structural Biology Consortium, Hodder, A.J., Shun-Shion, A.S., Williams, D.M., White, K.M., Rosales, R., Kehrer, T., Miorin, L., Moreno, E., Patel, A.H., Rihn, S., Khalid, M.M., Vallejo-Gracia, A., Fozouni, P., Simoneau, C.R., Roth, T.L., Wu, D., Karim, M.A., Ghoussaini, M., Dunham, I., Berardi, F., Weigang, S., Chazal, M., Park, J., Logue, J., McGrath, M., Weston, S., Haupt, R., Hastie, C.J., Elliott, M., Brown, F., Burness, K.A., Reid, E., Dorward,

M., Johnson, C., Wilkinson, S.G., Geyer, A., Giesel, D.M., Baillie, C., Raggett, S., Leech, H., Toth, R., Goodman, N., Keough, K.C., Lind, A.L., Zoonomia Consortium, Klesh, R.J., Hemphill, K.R., Carlson-Stevermer, J., Oki, J., Holden, K., Maures, T., Pollard, K.S., Sali, A., Agard, D.A., Cheng, Y., Fraser, J.S., Frost, A., Jura, N., Kortemme, T., Manglik, A., Southworth, D.R., Stroud, R.M., Alessi, D.R., Davies, P., Frieman, M.B., Ideker, T., Abate, C., Jouvenet, N., Kochs, G., Shoichet, B., Ott, M., Palmarini, M., Shokat, K.M., García-Sastre, A., Rassen, J.A., Grosse, R., Rosenberg, O.S., Verba, K.A., Basler, C.F., Vignuzzi, M., Peden, A.A., Beltrao, P., Krogan, N.J., 2020a. Comparative host-coronavirus protein interaction networks reveal pan-viral disease mechanisms. Science 370. https://doi.org/10.1126/science.abe9403

Gordon, D.E., Jang, G.M., Bouhaddou, M., Xu, J., Obernier, K., White, K.M., O'Meara, M.J., Rezelj, V.V., Guo, J.Z., Swaney, D.L., Tummino, T.A., Hüttenhain, R., Kaake, R.M., Richards, A.L., Tutuncuoglu, B., Foussard, H., Batra, J., Haas, K., Modak, M., Kim, M., Haas, P., Polacco, B.J., Braberg, H., Fabius, J.M., Eckhardt, M., Soucheray, M., Bennett, M.J., Cakir, M., McGregor, M.J., Li, Q., Meyer, B., Roesch, F., Vallet, T., Mac Kain, A., Miorin, L., Moreno, E., Naing, Z.Z.C., Zhou, Y., Peng, S., Shi, Y., Zhang, Z., Shen, W., Kirby, I.T., Melnyk, J.E., Chorba, J.S., Lou, K., Dai, S.A., Barrio-Hernandez, I., Memon, D., Hernandez-Armenta, C., Lyu, J., Mathy, C.J.P., Perica, T., Pilla, K.B., Ganesan, S.J., Saltzberg, D.J., Rakesh, R., Liu, X., Rosenthal, S.B., Calviello, L., Venkataramanan, S., Liboy-Lugo, J., Lin, Y., Huang, X.-P., Liu, Y., Wankowicz, S.A., Bohn, M., Safari, M., Ugur, F.S., Koh, C., Savar, N.S., Tran, Q.D., Shengjuler, D., Fletcher, S.J., O'Neal, M.C., Cai, Y., Chang, J.C.J., Broadhurst, D.J., Klippsten, S., Sharp, P.P., Wenzell, N.A., Kuzuoglu-Ozturk, D., Wang, H.-Y., Trenker, R., Young, J.M., Cavero, D.A., Hiatt, J., Roth, T.L., Rathore, U., Subramanian, A., Noack, J., Hubert, M., Stroud, R.M., Frankel, A.D., Rosenberg, O.S., Verba, K.A., Agard, D.A., Ott, M., Emerman, M., Jura, N., von Zastrow, M., Verdin, E., Ashworth, A., Schwartz, O., d'Enfert, C., Mukherjee, S., Jacobson, M., Malik, H.S., Fujimori, D.G., Ideker, T., Craik, C.S., Floor, S.N., Fraser, J.S., Gross, J.D., Sali, A., Roth, B.L., Ruggero, D., Taunton, J., Kortemme, T., Beltrao, P., Vignuzzi, M., García-Sastre, A., Shokat, K.M., Shoichet, B.K., Krogan, N.J., 2020b. A SARS-CoV-2 protein interaction map reveals targets for drug repurposing. Nature 583, 459–468. https://doi.org/10.1038/s41586-020-2286-9

Gupta, S., Ylä-Anttila, P., Sandalova, T., Achour, A., Masucci, M.G., 2020. Interaction With 14-3-3 Correlates With Inactivation of the RIG-I Signalosome by Herpesvirus Ubiquitin Deconjugases. Front. Immunol. 11, 437. https://doi.org/10.3389/fimmu.2020.00437

Harrell, E.K.T., Copeland, K., Prasad, M.D., Asundi, V., Hahner, N, Francis, J., Dey, D., Welsh, J.C., Macieik, A., Lingappa, J.R., Kelleher, C., Hurt, C.R., Hansen, W.J, 2010. Cell-Free Protein Synthesizing Systems As Tools for Discovery of Drugs Inhibiting Viral Capsid Assembly. Antiviral Res. 86, pA61.

Ingber, D.E., 2020. Is it Time for Reviewer 3 to Request Human Organ Chip Experiments Instead of Animal Validation Studies? Adv. Sci. Weinh. Baden-Wurtt. Ger. 7, 2002030. https://doi.org/10.1002/advs.202002030

Ison, M.G., 2011. Antivirals and resistance: influenza virus. Curr. Opin. Virol. 1, 563–573. https://doi.org/10.1016/j.coviro.2011.09.002

Jeffery, C.J., 2019. Multitalented actors inside and outside the cell: recent discoveries add to the number of moonlighting proteins. Biochem. Soc. Trans. 47, 1941–1948. https://doi.org/10.1042/BST20190798

Jia, H., Liang, Z., Zhang, X., Wang, J., Xu, W., Qian, H., 2017. 14-3-3 proteins: an important regulator of autophagy in diseases. Am. J. Transl. Res. 9, 4738–4746.

Jung, K., Saif, L.J., Wang, Q., 2020. Porcine epidemic diarrhea virus (PEDV): An update on etiology, transmission, pathogenesis, and prevention and control. Virus Res. 286, 198045. https://doi.org/10.1016/j.virusres.2020.198045

Kii, I., Sumida, Y., Goto, T., Sonamoto, R., Okuno, Y., Yoshida, S., Kato-Sumida, T., Koike, Y., Abe, M., Nonaka, Y., Ikura, T., Ito, N., Shibuya, H., Hosoya, T., Hagiwara, M., 2016. Selective

inhibition of the kinase DYRK1A by targeting its folding process. Nat. Commun. 7, 11391. https://doi.org/10.1038/ncomms11391

Koonin, E.V., Dolja, V.V., Krupovic, M., 2015. Origins and evolution of viruses of eukaryotes: The ultimate modularity. Virology 479–480, 2–25. https://doi.org/10.1016/j.virol.2015.02.039

Krupovic, M., Koonin, E.V., 2017. Multiple origins of viral capsid proteins from cellular ancestors. Proc. Natl. Acad. Sci. U. S. A. 114, E2401–E2410. https://doi.org/10.1073/pnas.1621061114

Leliveld, S.R., Korth, C., 2007. The use of conformation-specific ligands and assays to dissect the molecular mechanisms of neurodegenerative diseases. J. Neurosci. Res. 85, 2285–2297. https://doi.org/10.1002/jnr.21353

Lingappa, J.R., Hill, R.L., Wong, M.L., Hegde, R.S., 1997. A multistep, ATP-dependent pathway for assembly of human immunodeficiency virus capsids in a cell-free system. J. Cell Biol. 136, 567–581. https://doi.org/10.1083/jcb.136.3.567

Lingappa, J.R., Lingappa, V.R., Reed, J.C., 2021. Addressing Antiretroviral Drug Resistance with Host-Targeting Drugs-First Steps towards Developing a Host-Targeting HIV-1 Assembly Inhibitor. Viruses 13, 451. https://doi.org/10.3390/v13030451

Lingappa, J.R., Martin, R.L., Wong, M.L., Ganem, D., Welch, W.J., Lingappa, V.R., 1994. A eukaryotic cytosolic chaperonin is associated with a high molecular weight intermediate in the assembly of hepatitis B virus capsid, a multimeric particle. J. Cell Biol. 125, 99–111. https://doi.org/10.1083/jcb.125.1.99

Lingappa, U.F., Wu, X., Macieik, A., Yu, S.F., Atuegbu, A., Corpuz, M., Francis, J., Nichols, C., Calayag, A., Shi, H., Ellison, J.A., Harrell, E.K.T., Asundi, V., Lingappa, J.R., Prasad, M.D., Lipkin, W.I., Dey, D., Hurt, C.R., Lingappa, V.R., Hansen, W.J., Rupprecht, C.E., 2013. Host-rabies virus protein-protein interactions as druggable antiviral targets. Proc. Natl. Acad. Sci. 110, E861–E868. https://doi.org/10.1073/pnas.1210198110

Lingappa, V.R., Lingappa, J.R., 2005. Recent insights into biological regulation from cell-free protein-synthesizing systems. Mt. Sinai J. Med. N. Y. 72, 141–160.

Lingappa, V.R., Rutkowski, D.T., Hegde, R.S., Andersen, O.S., 2002. Conformational control through translocational regulation: a new view of secretory and membrane protein folding. BioEssays News Rev. Mol. Cell. Dev. Biol. 24, 741–748. https://doi.org/10.1002/bies.10130

Liu, J., Cao, S., Ding, G., Wang, B., Li, Y., Zhao, Y., Shao, Q., Feng, J., Liu, S., Qin, L., Xiao, Y., 2021. The role of 14-3-3 proteins in cell signalling pathways and virus infection. J. Cell. Mol. Med. 25, 4173–4182. https://doi.org/10.1111/jcmm.16490

Liu, J., Qian, C., Cao, X., 2016. Post-Translational Modification Control of Innate Immunity. Immunity 45, 15–30. https://doi.org/10.1016/j.immuni.2016.06.020

Lo, M.K., Nichol, S.T., Spiropoulou, C.F., 2014. Evaluation of luciferase and GFP-expressing Nipah viruses for rapid quantitative antiviral screening. Antiviral Res. 106, 53–60. https://doi.org/10.1016/j.antiviral.2014.03.011

Loo, S.-L., Wark, P.A.B., Esneau, C., Nichol, K.S., Hsu, A.C.-Y., Bartlett, N.W., 2020. Human coronaviruses 229E and OC43 replicate and induce distinct antiviral responses in differentiated primary human bronchial epithelial cells. Am. J. Physiol. Lung Cell. Mol. Physiol. 319, L926–L931. https://doi.org/10.1152/ajplung.00374.2020

Mao, J., Lin, E., He, L., Yu, J., Tan, P., Zhou, Y., 2019. Autophagy and Viral Infection. Adv. Exp. Med. Biol. 1209, 55–78. https://doi.org/10.1007/978-981-15-0606-2_5

McKimm-Breschkin, J.L., 2013. Influenza neuraminidase inhibitors: antiviral action and mechanisms of resistance. Influenza Other Respir. Viruses 7 Suppl 1, 25–36. https://doi.org/10.1111/irv.12047

Michi, A.N., Proud, D., 2021. A toolbox for studying respiratory viral infections using air-liquid interface cultures of human airway epithelial cells. Am. J. Physiol. Lung Cell. Mol. Physiol. 321, L263–L280. https://doi.org/10.1152/ajplung.00141.2021

Motlagh, H.N., Hilser, V.J., 2012. Agonism/antagonism switching in allosteric ensembles. Proc. Natl. Acad. Sci. U. S. A. 109, 4134–4139. https://doi.org/10.1073/pnas.1120519109

689 Movia, D., Prina-Mello, A., 2020. Preclinical Development of Orally Inhaled Drugs (OIDs)-Are Animal
690 Models Predictive or Shall We Move Towards In Vitro Non-Animal Models? Anim. Open
691 Access J. MDPI 10, E1259. https://doi.org/10.3390/ani10081259
692 Muthuri, S.G., Venkatesan, S., Myles, P.R., Leonardi-Bee, J., Al Khuwaitir, T.S.A., Al Mamun, A.,
693 Anovadiya, A.P., Azziz-Baumgartner, E., Báez, C., Bassetti, M., Beovic, B., Bertisch, B.,
694 Bonmarin, I., Booy, R., Borja-Aburto, V.H., Burgmann, H., Cao, B., Carratala, J., Denholm, J.T.,
695 Dominguez, S.R., Duarte, P.A.D., Dubnov-Raz, G., Echavarria, M., Fanella, S., Gao, Z.,
696 Gérardin, P., Giannella, M., Gubbels, S., Herberg, J., Iglesias, A.L.H., Hoger, P.H., Hu, X., Islam,
697 Q.T., Jiménez, M.F., Kandeel, A., Keijzers, G., Khalili, H., Knight, M., Kudo, K., Kusznierz, G.,
698 Kuzman, I., Kwan, A.M.C., Amine, I.L., Langenegger, E., Lankarani, K.B., Leo, Y.-S., Linko,
699 R., Liu, P., Madanat, F., Mayo-Montero, E., McGeer, A., Memish, Z., Metan, G., Mickiene, A.,
700 Mikić, D., Mohn, K.G.I., Moradi, A., Nymadawa, P., Oliva, M.E., Ozkan, M., Parekh, D., Paul,
701 M., Polack, F.P., Rath, B.A., Rodríguez, A.H., Sarrouf, E.B., Seale, A.C., Sertogullarindan, B.,
702 Siqueira, M.M., Skręt-Magierło, J., Stephan, F., Talarek, E., Tang, J.W., To, K.K.W., Torres, A.,
703 Törün, S.H., Tran, D., Uyeki, T.M., Van Zwol, A., Vaudry, W., Vidmar, T., Yokota, R.T.C.,
704 Zarogoulidis, P., PRIDE Consortium Investigators, Nguyen-Van-Tam, J.S., 2014. Effectiveness
705 of neuraminidase inhibitors in reducing mortality in patients admitted to hospital with influenza A
706 H1N1pdm09 virus infection: a meta-analysis of individual participant data. Lancet Respir. Med.
707 2, 395–404. https://doi.org/10.1016/S2213-2600(14)70041-4
708 Nijhuis, M., van Maarseveen, N.M., Boucher, C.A.B., 2009. Antiviral Resistance and Impact on Viral
709 Replication Capacity: Evolution of Viruses Under Antiviral Pressure Occurs in Three Phases, in:
710 Kräusslich, H.-G., Bartenschlager, R. (Eds.), Antiviral Strategies, Handbook of Experimental
711 Pharmacology. Springer Berlin Heidelberg, Berlin, Heidelberg, pp. 299–320.
712 https://doi.org/10.1007/978-3-540-79086-0_11
713 Nirenberg, M., 2004. Historical review: Deciphering the genetic code – a personal account. Trends
714 Biochem. Sci. 29, 46–54. https://doi.org/10.1016/j.tibs.2003.11.009
715 Obsilova, V., Obsil, T., 2020. The 14-3-3 Proteins as Important Allosteric Regulators of Protein Kinases.
716 Int. J. Mol. Sci. 21, E8824. https://doi.org/10.3390/ijms21228824
717 Peck, K.M., Lauring, A.S., 2018. Complexities of Viral Mutation Rates. J. Virol. 92.
718 https://doi.org/10.1128/JVI.01031-17
719 Pei, Z., Harrison, M.S., Schmitt, A.P., 2011. Parainfluenza virus 5 m protein interaction with host protein
720 14-3-3 negatively affects virus particle formation. J. Virol. 85, 2050–2059.
721 https://doi.org/10.1128/JVI.02111-10
722 Perrin-Cocon, L., Diaz, O., Jacquemin, C., Barthel, V., Ogire, E., Ramière, C., André, P., Lotteau, V.,
723 Vidalain, P.-O., 2020. The current landscape of coronavirus-host protein-protein interactions. J.
724 Transl. Med. 18, 319. https://doi.org/10.1186/s12967-020-02480-z
725 Petsch, B., Hurt, C.R., Freeman, B., Zirdum, E., Ganesh, A., Schörg, A., Kitaygorodskyy, A., Marwidi,
726 Y., Ducoudret, O., Kelleher, C., Hansen, W., Lingappa, V.R., Essrich, C., Stitz, L., 2010.
727 Discovery of Novel Small Molecule Inhibitors of Multiple Influenza Strains in Cell Culture.
728 Antiviral Res. 86, A42. https://doi.org/10.1016/j.antiviral.2010.02.398
729 Reed, J.C., Solas, D., Kitaygorodskyy, A., Freeman, B., Ressler, D.T.B., Phuong, D.J., Swain, J.V.,
730 Matlack, K., Hurt, C.R., Lingappa, V.R., Lingappa, J.R., 2021. Identification of an Antiretroviral
731 Small Molecule That Appears To Be a Host-Targeting Inhibitor of HIV-1 Assembly. J. Virol. 95.
732 https://doi.org/10.1128/JVI.00883-20
733 Song, L., Luo, Z.-Q., 2019. Post-translational regulation of ubiquitin signaling. J. Cell Biol. 218, 1776–
734 1786. https://doi.org/10.1083/jcb.201902074
735 Stevers, L.M., Sijbesma, E., Botta, M., MacKintosh, C., Obsil, T., Landrieu, I., Cau, Y., Wilson, A.J.,
736 Karawajczyk, A., Eickhoff, J., Davis, J., Hann, M., O'Mahony, G., Doveston, R.G., Brunsveld,
737 L., Ottmann, C., 2018. Modulators of 14-3-3 Protein-Protein Interactions. J. Med. Chem. 61,
738 3755–3778. https://doi.org/10.1021/acs.jmedchem.7b00574

Tanaka, A., 2009. Identification of the specific binding proteins of bioactive small compound using affinity resins. Methods Mol. Biol. Clifton NJ 577, 181–195. https://doi.org/10.1007/978-1-60761-232-2_14

Tugaeva, K.V., Hawkins, D.E.D.P., Smith, J.L.R., Bayfield, O.W., Ker, D.-S., Sysoev, A.A., Klychnikov, O.I., Antson, A.A., Sluchanko, N.N., 2021. The Mechanism of SARS-CoV-2 Nucleocapsid Protein Recognition by the Human 14-3-3 Proteins. J. Mol. Biol. 433, 166875. https://doi.org/10.1016/j.jmb.2021.166875

Umezawa, K., Kii, I., 2021. Druggable Transient Pockets in Protein Kinases. Mol. Basel Switz. 26, 651. https://doi.org/10.3390/molecules26030651

Uversky, V.N., 2016. Dancing Protein Clouds: The Strange Biology and Chaotic Physics of Intrinsically Disordered Proteins. J. Biol. Chem. 291, 6681–6688. https://doi.org/10.1074/jbc.R115.685859

Waghmare, A., Xie, H., Kuypers, J., Sorror, M.L., Jerome, K.R., Englund, J.A., Boeckh, M., Leisenring, W.M., 2019. Human Rhinovirus Infections in Hematopoietic Cell Transplant Recipients: Risk Score for Progression to Lower Respiratory Tract Infection. Biol. Blood Marrow Transplant. 25, 1011–1021. https://doi.org/10.1016/j.bbmt.2018.12.005

Watanabe, T., Kawakami, E., Shoemaker, J.E., Lopes, T.J.S., Matsuoka, Y., Tomita, Y., Kozuka-Hata, H., Gorai, T., Kuwahara, T., Takeda, E., Nagata, A., Takano, R., Kiso, M., Yamashita, M., Sakai-Tagawa, Y., Katsura, H., Nonaka, N., Fujii, H., Fujii, K., Sugita, Y., Noda, T., Goto, H., Fukuyama, S., Watanabe, S., Neumann, G., Oyama, M., Kitano, H., Kawaoka, Y., 2014. Influenza virus-host interactome screen as a platform for antiviral drug development. Cell Host Microbe 16, 795–805. https://doi.org/10.1016/j.chom.2014.11.002

Welch, S.R., Scholte, F.E.M., Harmon, J.R., Coleman-McCray, J.D., Lo, M.K., Montgomery, J.M., Nichol, S.T., Spiropoulou, C.F., Spengler, J.R., 2020. In Situ Imaging of Fluorescent Nipah Virus Respiratory and Neurological Tissue Tropism in the Syrian Hamster Model. J. Infect. Dis. 221, S448–S453. https://doi.org/10.1093/infdis/jiz393

WHO publishes list of top emerging diseases likely to cause major epidemics [WWW Document], 2015. . Httpswwwwhointnewsitem10-12-2015-Who-Publ.-List--Top-Emerg.-Dis.-Likely--Cause-Major-Epidemics. URL https://www.who.int/news/item/10-12-2015-who-publishes-list-of-top-emerging-diseases-likely-to-cause-major-epidemics

Williams, N.K., Dichtl, B., 2018. Co-translational control of protein complex formation: a fundamental pathway of cellular organization? Biochem. Soc. Trans. 46, 197–206. https://doi.org/10.1042/BST20170451

Xu, Y., Wu, W., Han, Q., Wang, Y., Li, C., Zhang, P., Xu, H., 2019. Post-translational modification control of RNA-binding protein hnRNPK function. Open Biol. 9, 180239. https://doi.org/10.1098/rsob.180239

Zhao, Z., Lu, K., Mao, B., Liu, S., Trilling, M., Huang, A., Lu, M., Lin, Y., 2021. The interplay between emerging human coronavirus infections and autophagy. Emerg. Microbes Infect. 10, 196–205. https://doi.org/10.1080/22221751.2021.1872353

Acknowledgments:

We thank Alfredo Calayag, Lisa Tucker, Caleb Declouette, Yvonne Dickschen, and Björn Wefers for excellent technical assistance, David Hanzel for careful reading and improvement of the manuscript, and Dmitry Temnikov for IT support. We are indebted to the late Guenter Blobel for advice, inspiration, and encouragement.

Funding:

Funding for this work was provided by Prosetta Biosciences Inc. A.M.S. and C.K. are funded by a grant from the Deutsche Forschungsgemeinschaft (KO1679/15-1).

Author contributions:

Experiments: MM, DL, JC, SFY, AM, VRL, AMS, SB, AFL, EMB, OA, JL, FD, IJ, DG, ARM, IB, SL, IS, MF, ND, CN, JR, JRL, DD, KM, MF, NSP, MF, MJF, KC, MKL.

Reagents and method development: UA, VA, SH, AFL, AMS, KM, MM, SY, KC, LM, PNO, MA, JCR, JRL, OA, HS, IJ, MKL.

Synthetic chemistry: KP, DS, AK.

Analysis and interpretation: UFL, AFL, VRL, EP, CN, TWC, SKA, SS, RAT, RJH, SM, DP, MJF, AMS, CK, BO, JG, SP, MKL, CFS, JMM.

Writing: HB, UFL, CK, AMS, VRL.

Competing interests:
VRL is CEO of Prosetta Biosciences.

Disclaimer Statement:
The findings and conclusions in this report are those of the authors and do not necessarily represent the views of the Centers for Disease Control and Prevention.

Data availability:
All data are included in the main text or supplementary materials.

Ethics:
De-identified human airway tissue samples were obtained from an Institutional Review Board approved biobank at UCSF (protocol #13-10738). All animal studies were approved by Institutional Animal Care and Use Committees.

Supplementary Materials
Materials and Methods
Figures S1 to S6
Table S1

Materials and Methods

Materials

Materials were purchased from Sigma Chemical Co. or Thermo Fisher, unless otherwise noted. Selected antibodies were purchased from Bethyl Laboratories, Inc (rabbit polyclonal affinity purified antibody to VCP/p97, catalog number A300-588A-T), Abcam (mouse monoclonal antibody to p62, catalog number ab56416), Santa Cruz (rabbit polyclonal pan 14-3-3 antibody catalog number SC-1657), LSBio (rabbit polyclonal antibody to CAPN2, catalog number LS-C400613).

CFPSA screen

Coding regions of interest were engineered behind the SP6 bacteriophage promoter and the Xenopus globin 5′ UTR63. DNA was amplified by PCR and then transcribed in vitro to generate mRNA encoding each full-length protein. Translations were carried out in wheat germ extracts supplemented with energy and amino acids, as previously described(*7*). Moderate-throughput small molecule screening was carried out in 384-well plate format by translation of eGFP and FLUV NP and M mRNA in the presence of small molecules from the Prosetta compound collection (Figure S2). Reactions were run at 26°C for 1-2 hours for synthesis, followed by assembly at 34°C for 2 hours. eGFP fluorescent readout was measured at 488/515 nm (excitation/emission) to assess protein synthesis. Assembly products were captured on a second 384-well plate precoated with affinity-purified FLUV NP antibody. Plates were washed with PBS containing 1% Triton X-100, decorated with biotinylated affinity-purified FLUV NP antibody, washed, detected by NeutraAvidin HRP, washed again, and then incubated with a fluorogenic HRP substrate Quanta Blue for 1 hour. FLUV assembly fluorescent readout was measured at 330/425 nm (excitation/emission).

FLUV assay in MDCK cells

MDCK.2 cells were seeded at $3x10^4$ cells/well in Eagle's minimal essential medium (MEM) supplemented with fetal bovine serum (FBS) in a 96-well plate and incubated overnight at 37°C. The next

day, cells were washed with phosphate buffered saline (PBS) and infected with FLUV A/WSN/33 at an MOI of 0.01-0.001 for 1 hour, after which the virus containing media was removed and fresh media containing dilutions of compound or DMSO as a vehicle control was added to the cells. After 24 hours, media was removed, cells were washed with PBS, and fresh media was added for a 2 hour incubation and then collected for $TCID_{50}$ determination. Seven replicates of 10-fold serial dilutions of collected media were added to new cells and incubated at 37°C for 3 days. The number of infected wells for each dilution was determined by visual inspection, and $TCID_{50}$/mL was calculated using the Reed and Muench method(*37*). Infection experiments were conducted in a BSL2 laboratory.

BoCoV assay in HRT-18G cells

HRT-18G cells were seeded at $3x10^4$ cells/well in Dulbecco's modified Eagle medium (DMEM) in a 96-well plate and incubated overnight at 37°C. The next day, cells were infected with BoCoV BRCV-OK-0514-2 (ATCC VR-2460) at an MOI of 1 for 2 hours, after which the virus containing media was removed, cells were washed with PBS, and fresh media containing dilutions of compound or DMSO as a vehicle control was added to the cells. After 42-48 hours, media was removed, cells were washed with PBS, and fresh media was added for a 4 hour incubation and then collected for $TCID_{50}$ determination. Infection experiments were conducted in a BSL2 laboratory.

HRV assay in H1-HeLa cells

H1-HeLa cells were seeded at $7x10^4$ cells/well in MEM in a 96-well plate and incubated overnight at 37°C. The next day, cells were infected with HRV-16 at an MOI of 5 for 1.5 hours, after which the virus containing media was removed, cells were washed with PBS, and fresh media containing dilutions of compound or DMSO as a vehicle control was added to the cells. After 72 hours, media was collected for $TCID_{50}$ determination. Infection experiments were conducted in a BSL2 laboratory.

MHV assay in BHK-21 cells

BHK-21 cells were seeded at $2.5x10^5$ cells/well in MEM in a 96-well plate and incubated overnight at 37°C. The next day, cells were infected with MHV-68 at an MOI of 0.5 for 1.5-2 hours, after which the virus containing media was removed, cells were washed with PBS, and fresh media containing dilutions of compound or DMSO as a vehicle control was added to the cells. After 24 hours, media was removed, cells were washed with PBS, and fresh media was added for a 4 hour incubation and then collected for $TCID_{50}$ determination. Infection experiments were conducted in a BSL2 laboratory.

SARS-CoV-2 assay in Vero cells

Vero clone E6 (CRL-1586) cells were plated at $3x10^5$ cells/well in DMEM in 6-well plates and incubated overnight at 37ºC. The next day, cells were washed once with PBS and then infected with SARS-CoV-2 WA1/2020 (MN985325.1, BEI resources) at a MOI of 0.01 for 1 hour after which the virus containing media was removed and the compounds were added to the cells and incubated for 72 hours at 37ºC at 5% CO_2. The cells were then fixed and stained with crystal violet to determine plaque numbers(*38*). Infection experiments were conducted in a BSL3 laboratory. Data shown in Figure 4B are the averages of two biological replicates; error bars indicate standard error; DMSO is included as the vehicle control.

SARS-CoV-2 (delta) assay in Calu-3 cells

Calu-3 cells were seeded at a density of $3x10^4$ cells/well in DMEM in 96-well plates and incubated overnight at 37°C. The next day, cells were pre-incubated with compounds for 4 hours before they were infected with SARS-CoV-2 delta SL102 (EPI_ISL_4471559) at a MOI of 0.01-0.05. After 24 hours the viruses within 50 µl of the supernatants were lysed with 200 µL AVL-buffer (Qiagen) and 200 µL 100% ethanol was added for complete inactivation. RNA was extracted from 200 µL of the lysates using the EZ1 Virus Mini-Kit (Qiagen), and analyzed by qPCR as described(*39*). Infection experiments

were conducted in a BSL3 laboratory. Data shown are the averages of three biological replicates; error bars indicate standard error; DMSO is included as the vehicle control.

Cell culture for Nipah virus studies

Human telomerase reverse-transcriptase immortalized primary-like small airway epithelial cells (HSAEC1-KT, ATCC CRL-4050) were cultured in Airway Epithelial Basal Medium (ATCC) supplemented with Bronchial Epithelial Cell Growth Kit (ATCC) as previously described (Lo et al., 2020 AVR). For infections and cell viability assays, HSAEC1-KT cells were cultured with growth medium either with or without 5 mM of D-glucose solution (Gibco).

Recombinant ZsGreen-expressing Nipah virus infection

HSAEC1-KT cells were seeded at 10,000 cells per well the day prior to infection in 96-well black plates with clear bottoms (Costar 3603). The following day, cells were infected with recombinant Nipah virus expressing ZsGreen fluorescence protein (rNiV-ZsG) (Lo et al., 2014, 2018, 2020 AVR: Welch et al., 2020 JID) at multiplicity of infection 0.01 with ~ 100 50% tissue culture infectious dose ($TCID_{50}$). Levels of rNiV-ZsG replication were measured at 72 hour post-infection based on mean ZsGreen fluorescence signal intensity ($418_{ex}/518_{em}$) using a Biotek HD1 Synergy instrument (Aglilent). Fluorescence signal intensity assayed in DMSO-treated, virus-infected cells were set as 100% ZsGreen fluorescence. Data points and error bars for all reporter assays indicate the mean value and standard deviation of 4 biological replicates, and are representative of at least 2 independent experiments in HSAEC1-KT cells. Concentrations of compound that inhibited 50% of the green fluorescence signal (EC_{50}) were calculated from dose response data fitted to the mean value of experiments performed for each concentration in the 10-point, 3-fold dilution series using a 4-parameter non-linear logistic regression curve with variable slope using GraphPad Prism 9 (GraphPad Software, La Jolla, CA, USA).

933 *CellTiterGlo cell viability assay*

934 Cell viability was assayed using CellTiter-Glo 2.0 assay reagent (Promega) according to manufacturer's
935 recommendations, with luminescence measured at 72 hours post-compound treatment using a Biotek
936 HD1 Synergy instrument. Luminescence levels (indicative of cellular ATP levels as a surrogate marker of
937 cell viability) assayed in DMSO-treated, uninfected cells were set as 100% cell viability. Dose response
938 curves were fitted to the mean value of experiments performed for each concentration in the 10-point, 3-
939 fold dilution series using a 4-parameter non-linear logistic regression curve with variable slope. All
940 CellTiter-Glo cell viability assays were conducted in 96-well opaque white plates (Costar 3917).
941 Concentrations of compound that inhibited 50% of the luminescence signal (CC_{50}) were calculated from
942 dose response data fitted to the mean value of experiments performed for each concentration in the 10-
943 point, 3-fold dilution series using a 4-parameter non-linear logistic regression curve with variable slope
944 using GraphPad Prism 9 (GraphPad Software, La Jolla, CA, USA).
945
946 *Alamar Blue HS cell viability assay*
947 Cell viability was assayed using Alamar Blue HS reagent (Thermofisher) according to manufacturer's
948 recommendations, with fluorescence ($560_{ex}/590_{em}$) measured at 72 hours post-compound treatment after 4
949 hours of incubation with reagent using a Biotek HD1 Synergy instrument. Fluorescence levels (indicative
950 of resazurin reduction as a surrogate marker of cell viability) assayed in DMSO-treated, uninfected cells
951 were set as 100% cell viability. Dose response curves were fitted to the mean value of experiments
952 performed for each concentration in the 10-point, 3-fold dilution series using a 4-parameter non-linear
953 logistic regression curve with variable slope. All Alamar Blue assays were conducted in 96-well black
954 plates with clear bottoms. Concentrations of compound that inhibited 50% of the fluorescence signal
955 (CC_{50}) were calculated from dose response data fitted to the mean value of experiments performed for
956 each concentration in the 10-point, 3-fold dilution series using a 4-parameter non-linear logistic
957 regression curve with variable slope using GraphPad Prism 9 (GraphPad Software, La Jolla, CA, USA).
958

PEDV pig study

18 litters comprised of 91 individuals of newborn (2 – 4 days old) crossbred pigs weighing 3 kg were randomized to control (vehicle) or treatment groups. Animals were infected with $1x10^5$ PFU of PEDV administered orally. Vehicle or drug was administered intramuscular at 4 mg/kg immediately after challenge and again 24 hours post-infection. Compound efficacy was determined by survivability. Endpoint of study was 6 days post-infection.

RSV cotton rat study

Female cotton rats, ~5 weeks of age, were obtained from Envigo (formerly Harlan), ear-tagged for identification purposes, and allowed to acclimate for > 1 week prior to study start. Animals were housed individually. Vehicle or drug was administered by an intraperitoneal route twice daily on study days -1 through day 4. On day 0, animals were infected with $1x10^5$ PFU of RSV A-2 virus originally obtained from ATCC (VR-1540), administered in a 50 mL volume by an intranasal route approximately 2 hours after the morning treatment dose. Back titration of the viral stock and diluted inoculum was performed to confirm the titer of the RSV stock used for infection. All inoculations were performed while the animals were under the influence of inhalant anesthesia. All animals were euthanized on day 5 and the lungs were processed for determination of RSV titers by plaque assay.

Cell lysate preparation for eDRAC

Cells or tissues were extracted with PB buffer (10 mM Tris pH 7.6, 10 mM NaCl, 0.1 mM EDTA, and 0.35% Triton X-100), and centrifuged at 10,000 x g for 10 min. The supernatants were collected and flash frozen for later use.

eDRAC

Drug resin was prepared by coupling compound PAV-431 to an Affi-gel resin at a concentration of 10 µM via the pyrazole nitrogen (Figure S6, synthetic chemistry described below), or position 4 of the

phenyl group. Control resin was prepared by blocking the Affi-gel matrix without drug. Resins were equilibrated with column buffer (50 mM HEPES, pH 7.6, 100 mM KAc, 6 mM MgAc, 1 mM EDTA, 4 mM TGA) prior to any DRAC experiments. 30 µL of cell extract supplemented with energy (1 mM ATP, GTP, CTP and UTP with 4 mM creatine phosphate, and in some cases 5 µg/ml rabbit creatine kinase) was applied to resin columns. The columns were clamped and incubated at 22°C for 1 hour for binding, and flow through was collected. The columns were then washed with 100 bed volumes of column buffer. For elution of bound complexes, 100 µL of column buffer containing free drug at a final concentration of 100 µM – 1 mM (approaching its maximum solubility in water) and supplemented with energy was added, the column was clamped for 1 hour, and serial eluates were collected. Eluates were analyzed by SDS-PAGE and WB.

Western blotting

SDS-PAGE gels were transferred in Towbin buffer to a polyvinylidene fluoride membrane. Membranes were then blocked in 1% BSA, incubated for 1 hour at room temperature in a 1:1000 dilution of 100 µg/mL affinity-purified primary antibody, washed three times in PBS with 0.1% Tween-20, incubated for 1 hour in a 1:5000 dilution of secondary anti-rabbit or anti-mouse antibody coupled to alkaline phosphatase, washed further, and incubated in developer solution prepared from 100 µL of 7.5 mg/mL 5-bromo-4-chloro-3-indolyl phosphate dissolved in 60% dimethyl formamide (DMF) in water and 100 µL of 15 mg/mL nitro blue tetrazolium dissolved in 70% DMF in water, adjusted to 50 mL with 0.1 M Tris (pH 9.5)/0.1 mM magnesium chloride.

MS-MS analysis

Samples were processed by SDS-PAGE using a 10% Bis-Tris NuPAGE gel (Invitrogen) with the MES buffer system. The mobility region was excised and processed by in-gel digestion with trypsin using a ProGest robot (Digilab) with the protocol outlined below. Washed with 25 mM ammonium bicarbonate followed by acetonitrile. Reduced with 10 mM dithiothreitol at 60°C followed by alkylation with 50 mM

iodoacetamide at room temperature. Digested with trypsin (Promega) at 37°C for 4 hours. Quenched with formic acid, lyophilized, and reconstituted in 0.1% trifluoroacetic acid.

Half of each digested sample was analyzed by nano LC-MS/MS with a Waters M-Class HPLC system interfaced to a ThermoFisher Fusion Lumos mass spectrometer. Peptides were loaded on a trapping column and eluted over a 75 μm analytical column at 350 nL/min; both columns were packed with Luna C18 resin (Phenomenex). The mass spectrometer was operated in data-dependent mode, with the Orbitrap operating at 60,000 FWHM and 15,000 FWHM for MS and MS/MS respectively. APD was enabled and the instrument was run with a 3 s cycle for MS and MS/MS.

Data were searched using a local copy of Mascot (Matrix Science) with the following parameters: Enzyme: Trypsin/P; Database: SwissProt Human plus the custom sequences* (concatenated forward and reverse plus common contaminants); Fixed modification: Carbamidomethyl (C)Variable modifications: Oxidation (M), Acetyl (N-term), Pyro-Glu (N-term Q), Deamidation (N/Q)Mass values: Monoisotopic; Peptide Mass Tolerance: 10 ppm; Fragment Mass Tolerance: 0.02 Da; Max Missed Cleavages: 2. The data was analyzed by label free quantitation (LFQ) methods(*40*). LFQ intensity values of each condition were measured in triplicate and compared against each other to generate $\log_2$ fold change values for each protein and each combination of conditions. Proteins that were found significantly enriched by a $\log_2$ fold change of > 1 and an adjusted *p*-value (accounting for multiple hypothesis testing) of < 0.05 in the FLUV infected eDRAC eluates compared to the uninfected eluates were searched for in a list of high confidence FLUV virus-host protein interactions(*14*) and the VirusMentha database of virus-protein interactions(*41*). Likewise, significantly enriched and depleted proteins found in the BoCoV infected eDRAC eluate were searched for in a list of high confidence coronavirus interactors(*12*) and an aggregated list of coronavirus protein interactors shown experimentally(*13*).

Photocross-linking and streptavidin precipitation

eDRAC columns were eluted with 100μM PAV-431 photocross-linker at 22°C. Eluates were crosslinked by exposure to UV light for 3 minutes. Crosslinked products were subjected to treatments that

maintained protein-protein associations (native) or which reduced and denatured all proteins (denatured). Native conditions were maintained by diluting an aliquot of the product 20x with 1% Triton-X-100 column buffer. Denaturation was achieved by adjusting an aliquot to 1% SDS and 10mM DTT and heating to 100^{o}C/10 minutes prior to 20x dilution with 1% Triton-X-100 column buffer. Streptavidin Sepharose beads were added to both native and denatured samples and mixed for 1 hr to capture all biotinylated proteins, with and without co-associated proteins in the native and denatured cases respectively, then washed 3x with 1% Triton-containing column buffer. Washed beads were resuspended in 20µl of SDS loading buffer and analyzed by SDS-PAGE and WB.

Primary airway epithelial cell culture

Human bronchus was harvested from 3 explanted lungs. The tissue was submerged and agitated for 1 minute in PBS with antibiotics and 5mM dithiothreitol to wash and remove mucus. After 3 washes, the tissue was placed in DMEM with 0.1% protease and antibiotics overnight at 4°C. The next day the solution was agitated and remaining tissue removed. Cells were centrifuged at 300g/4°C for 5 minutes, then resuspended in 0.05% trypsin-EDTA and incubated for 5 minutes at 37°C. The trypsinization reaction was neutralized with 10% FBS in DMEM, then cells were filtered through a cell strainer and centrifuged at 300g/4°C for 5 minutes. The cell pellet was resuspended in 10% FBS in DMEM and a 10uL aliquot was stained with trypan-blue and counted on a hemocytometer. $7.5x10^4$ cells were plated onto each 6mm/0.4mm FNC-coated Transwell air-liquid interface (ALI) insert. 10% FBS in DMEM and ALI media were added in equal volumes to each basal compartment and cultures were incubated at 37°C/5% CO_2. The next day, media was removed and both compartments were washed with PBS and antibiotics. ALI media was then added to each basal compartment and changed every 3 days until cells were ready for use at day 28.

All studies involving SARS-CoV-2 infection of primary airway epithelial cells were conducted in the Vitalant Research Institute BSL3 High-Containment Facility. 6 hours prior to infection, ALI medium containing dilutions of drugs (100nM) or DMSO was added to the basal compartment. For infection, ALI medium containing drugs was removed, and SARS-CoV-2 diluted in ALI-culture medium containing drugs (100nM, MOI=0.1) was added on to the apical chamber of inserts (250 µl) and the basal compartment (500 µl). The cultures were incubated for 2 hours at 37□/5% CO_2 to allow for virus entry, then washed, and 500 µl of fresh ALI medium containing drugs (100 nM) was added to the basal compartment. Drugs were maintained in the medium for the duration of the experiment. Cells were incubated at 37□/5% CO_2 and harvested for analysis at 36 hours post-infection.

Total RNA was extracted from mock and SARS-CoV-2-infected primary airway epithelial cells with or without drug treatment lysed in Trizol (Thermo Fisher Scientific) using the chloroform-isopropanol-ethanol method. 500 ng of RNA was reversed transcribed into cDNA in 20 uL reaction volume using RevertAid First Strand cDNA Synthesis kit (Thermo Fisher) in accordance to the manufacturer's guidelines. RT-PCR was performed for each sample using Taqman™ Universal Master Mix II, with UNG (Thermo Fisher) on the ViiA7 Real time PCR system. Primers and probes (2019-nCoV RUO kit) for detection of the SARS-CoV-2 Nucleocapsid (N) gene were obtained from IDT.

Synthesis of PAV-431

Synthetic schemes are illustrated in Figure S6. To a solution of 2-methoxy-3-trifluoromethoxy-benzaldehyde **1** (2.14 g, 9.71 mmol, 1.0 eq) in toluene (20 mL) was added 2,4-dimethoxybenzyl amine **2** (1.78 g, 10.68 mmol, 1.1 eq) and the reaction mixture was stirred at room temperature for 24 hours. Toluene was removed to give a residue, which was taken in MeOH (20 mL) and then $NaBH_4$ (735 mg, 19.42 mmol, 2.0 eq) was added slowly. The reaction mixture was stirred at room temperature for 6 hours. The solvent was removed and the residue was extracted in ethyl acetate and stirred with saturated aq $NaHCO_3$ for 1 hour. The organic layer was collected, dried, and the solvent was removed to give the

crude amine **3**, which was used in the next step without further purification. To a solution of the crude amine **3** (4.86 mmol, 1.0 eq) in DMF (20 mL) were added the acid **4** (888 mg, 5.35 mmol, 1.1 eq), DIEA (3.13 g, 24.3 mmol, 5eq) and HBTU (2.22 g, 5.83 mmol, 1.2 eq) and the reaction mixture was stirred at room temperature for 12 hours. The reaction mixture was then diluted with ethyl acetate (75 mL) and washed with 10% aq HCl (1 x 50 mL), sat $NaHCO_3$ (1 x 50 mL) and water (4 x 50 mL). The organic layer was collected, dried ($MgSO_4$) and evaporated to give a crude product, which was purified by column chromatography (EtOAc:Hexane 25%:75%)) to give the amide **5**, which was directly used in the next step. The amide **5** was treated with 95% TFA:H_2O for 12 hours. TFA was removed and azeotroped with toluene to give a residue, which was purified by column chromatography (EtOAc:Hexane 10%:50%) to give PAV-431 (985 mg, > 95% purity).

Synthesis of PAV-431 resin

To a solution of amine **3** (5.85 g, 15.77 mmol, 1.0 eq) in DMF (30 mL) were added the acid **6** (2.38 g, 15.77 mmol, 1.0 eq), DIEA (10.2 g, 78.85 mmol, 5eq) and HBTU (7.17 g, 18.92 mmol, 1.2 eq) and the reaction mixture was stirred at room temperature for 12 hours. The reaction mixture was then diluted with ethyl acetate (75 mL) and washed with 10% aq HCl (1 x 50 mL), sat $NaHCO_3$ (1 x 50 mL) and water (4 x 50 mL). The organic layer was collected, dried ($MgSO_4$) and evaporated to give a crude product, which was purified by column chromatography (EtOAc/Hexane) to give compound **7**. To a stirred solution compound **7** (0.8 g, 1.77 mmol, 1.0 eq) and cesium carbonate (1.15 g, 3.54 mmol, 2.0 eq) in DMF (10 mL) was added chloride **8** (0.55 g, 2.66 mmol, 1.5 eq) and the reaction mixture was stirred at room temperature for 24 hours. The reaction mixture was diluted with ethyl acetate and washed with water (4x) and aq NaCl solution. The organic layer was collected, dried (MgSO4) and evaporated to give a crude product, which was purified by column chromatography (EtOAc/Hexane) to give compound **9**. The amide **9** (1.0 g, 1.6 mmol) was taken in 95% TFA: H_2O and the reaction mixture was for 12 hours. TFA was removed and azeotroped with toluene to give a residue. The residue was taken in DCM and sat. $NaHCO_3$ solution added and stirred for 30 min. The aqueous layer was washed with DCM (2x) and the

combined organic layer, dried ($MgSO_4$) and evaporated to give a crude amine, which was used in the next step without purification. To a solution of the crude amine (1.6 mmol, 1.0 eq) and DIEA (412.8 mg, 3.2 mmol, 2.0 eq) in DCM (20 mL), was added boc anhydride (523.2 mg, 2.4 mmol, 1.5 eq) and the reaction mixture was stirred at room temperature for 8 hours. The solvent was removed and the residue was purified by column chromatography (EtOAc/Hexane) to give compound **10**. Compound **10** (100 mg, 0.19 mmol) was in 5 mL of DCM and then 4 M HCl in dioxane (3 mL, 12 mmol) was added and the reaction mixture was stirred for 12 hours. Solvents were removed to give compound **11** as a HCl salt, which was used in the next step without further purification. To a solution of Affi-Gel 10 (Bio-Rad, 2 ml, 0.03 mmol, 1.0 eq) in a solid phase synthesis tube with frit was added a solution of compound **11** (27.7 mg, 0.06 mmol, 2.0 eq) and DIEA (1.0 mL) in isopropyl alcohol (4 mL) and the tube was put in a shaker for 12 hours. Excess reagents were drained and the resin was washed with isopropyl alcohol (3x) and then saved in isopropyl alcohol.

Synthesis of PAV-431 photocross-linker

To 6-(tert-Butoxycarbonylamino)-2-(9H-fluoren-9-ylmethoxycarbonylamino)hexanoic acid **12** [468mg (1mmol)] in a 40ml screw top vial was added 4N HCl in Dioxane (3ml). The vial was sealed and gently agitated for 20 minutes at room temperature. The mix was then rotary evaporated to dryness and the residue placed under high vacuum overnight. The dried residue was taken up into 4ml of DMF (anhydrous) and then sequentially treated with 3-(3-Methyldiazirin-3-yl)propanoic acid [128mg (1mmol)](*42*), and DIEA [695ul (4mmol)]. With rapid stirring, under Argon atmosphere, was added dropwise HATU [380mg (1mmol)] dissolved in 1ml of DMF. After stirring for 30 minutes the mixture was quenched with 10ml of sat. NH_4Cl solution and then extracted 2 x with 10ml of EtOAc. The combined organic extracts were washed once with sat. NaCl, dried (Mg_2SO_4) and then rotary evaporated to dryness. The residue was purified by flash chromatography, using a gradient of Ethyl acetate and Hexane, affording 2-(9H-fluoren-9-ylmethoxycarbonylamino)-6-[3-(3-methyldiazirin-3-yl)propanoylamino]hexanoic acid **13** (293mg) in 61% yield.

To tert-Butyl N-[3-[3-cyclopropyl-5-[[2-methoxy-3-(trifluoromethoxy)phenyl]methylcarbamoyl]pyrazol-1-yl]propyl]-N-methyl-carbamate **14** [16mg (0.03 mmol)] in a 40ml screw top vial was added 4N HCl in Dioxane (0.5ml). The vial was sealed and gently agitated for 20min at room temperature. The mix was then rotary evaporated to dryness and the residue placed on high vacuum overnight. The dried residue was taken up into 1ml of DMF (anhydrous) and then sequentially treated with compound **13** [14.5mg (0.03mmol)], and DIEA [32ul (0.18mmol)]. With rapid stirring, under Argon atmosphere, was added dropwise HATU [14.6mg (0.038mmol)] dissolved in 300ul of DMF. After stirring for 30 min the mixture was quenched with 5ml of sat. NH_4Cl solution and then extracted 2 x with 5ml of EtOAc.

The combined organic extracts were washed once with sat. NaCl, dried (Mg_2SO_4) and then rotary evaporated to dryness. The residue was purified by flash chromatography, using a gradient of Ethyl acetate and Hexane, affording 9H-fluoren-9-ylmethyl N-[1-[3-[3-cyclopropyl-5-[[2-methoxy-3-(trifluoromethoxy)phenyl]methylcarbamoyl]pyrazol-1-yl]propyl-methyl-carbamoyl]-5-[3-(3-methyldiazirin-3-yl)propanoylamino]pentyl]carbamate **15** (28mg) in quantitative yield.

To compound **15** [28mg (0.03 mmol)] in a 40ml screw top vial was added 50/50 Diethylamine / DMF (0.5ml). The vial was sealed and gently agitated for 60min at room temperature. The mix was then rotary evaporated to dryness and the residue placed on high vacuum overnight. The residue was triturated 2 x with 3ml of Hexane to remove the Dibenzofulvene amine adduct. The residue was again briefly placed on high vacuum to remove traces of Hexane. The dried residue was taken up into 1ml of DMF (anhydrous) and then treated with Biotin-PEG2-NHS [15mg (0.03mmol)] (purchased from ChemPep), and DIEA [16ul (0.09mmol)] and then purged with Argon. After stirring overnight at room temperature, the mixture was rotary evaporated to dryness. The residue was purified by reverse phase prep chromatography, using a gradient of 0.1% TFA water and Acetonitrile, affording 5-cyclopropyl-N-[[2-methoxy-3-(trifluoromethoxy)phenyl]methyl]-2-[3-[methyl-[6-[3-(3-methyldiazirin-3-yl)propanoylamino]-2-[3-[2-[2-[5-(2-oxo-1,3,3a,4,6,6a-hexahydrothieno[3,4-d]imidazol-4-

yl)pentanoylamino]ethoxy]ethoxy]propanoylamino]hexanoyl]amino]propyl]pyrazole-3-carboxamide (26mg) in 80% yield. All compounds were confirmed by LCMS.

Supplementary Figures and Legends

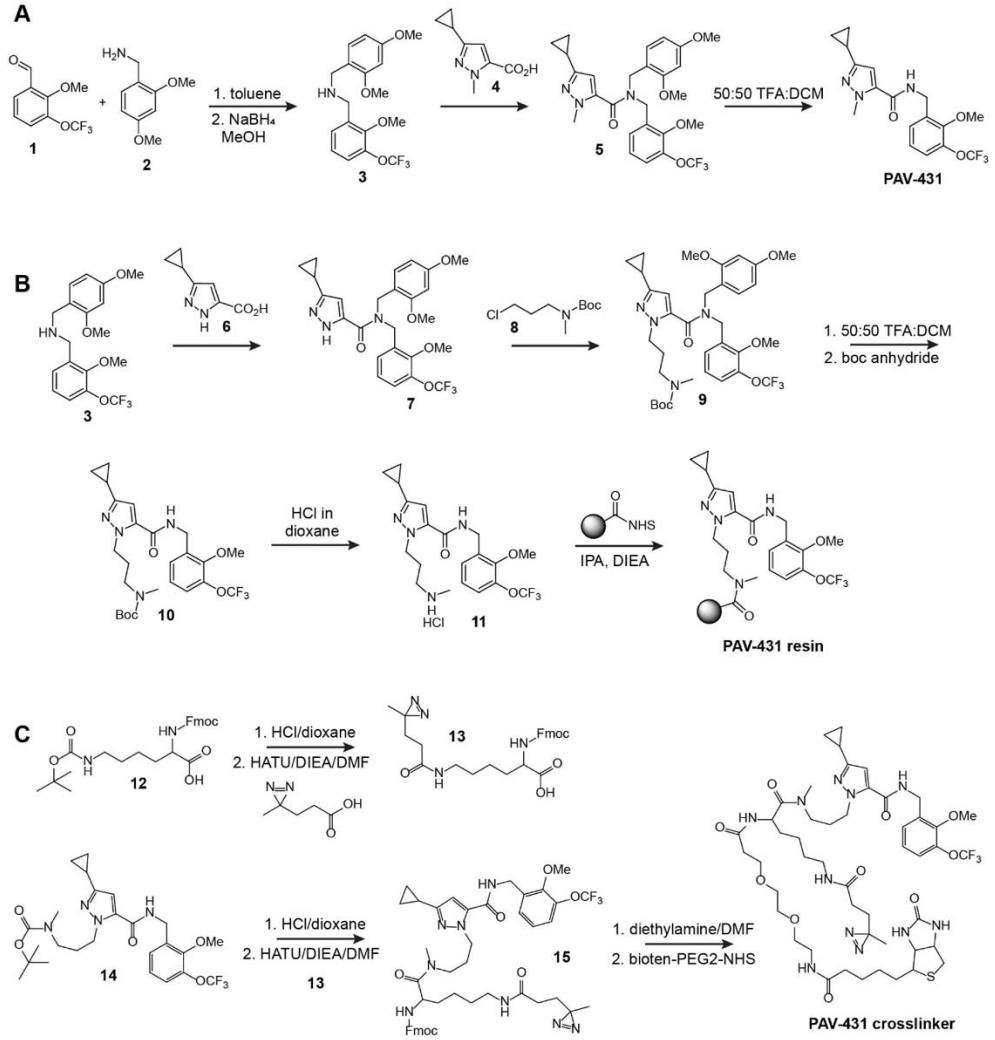

Supplementary Figure S1. General scheme for the synthesis of pyrazole carboxamides. (**A**) Preparation of PAV-431. (**B**) Preparation of PAV-431 resin. (**C**) Preparation of PAV-431 photocross-linker. Methodological details for these syntheses are described in Materials and Methods.

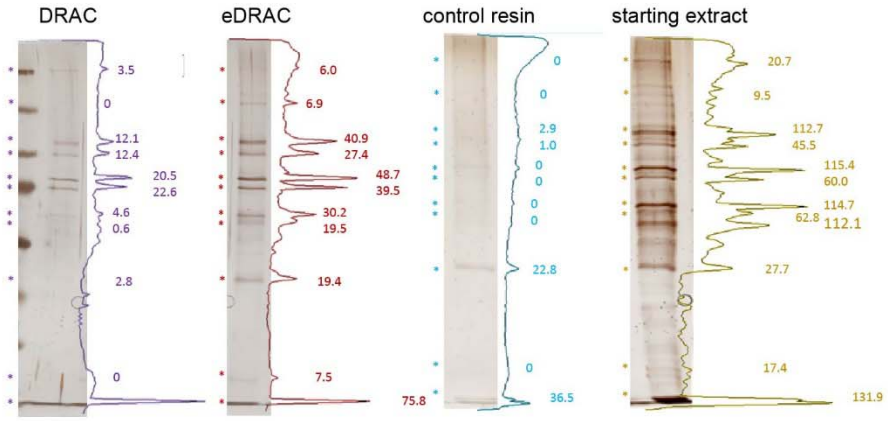

Supplementary Figure S2. eDRAC (DRAC supplemented with metabolic energy) shows a significant increase in target yield, demonstrated by eluates from extracts of MDCK cells analyzed by SDS-PAGE and silver stain showing the full target complex banding pattern. Lane profile traces and peak numbers indicate peak band densities, stars indicate bands present in eDRAC eluate.

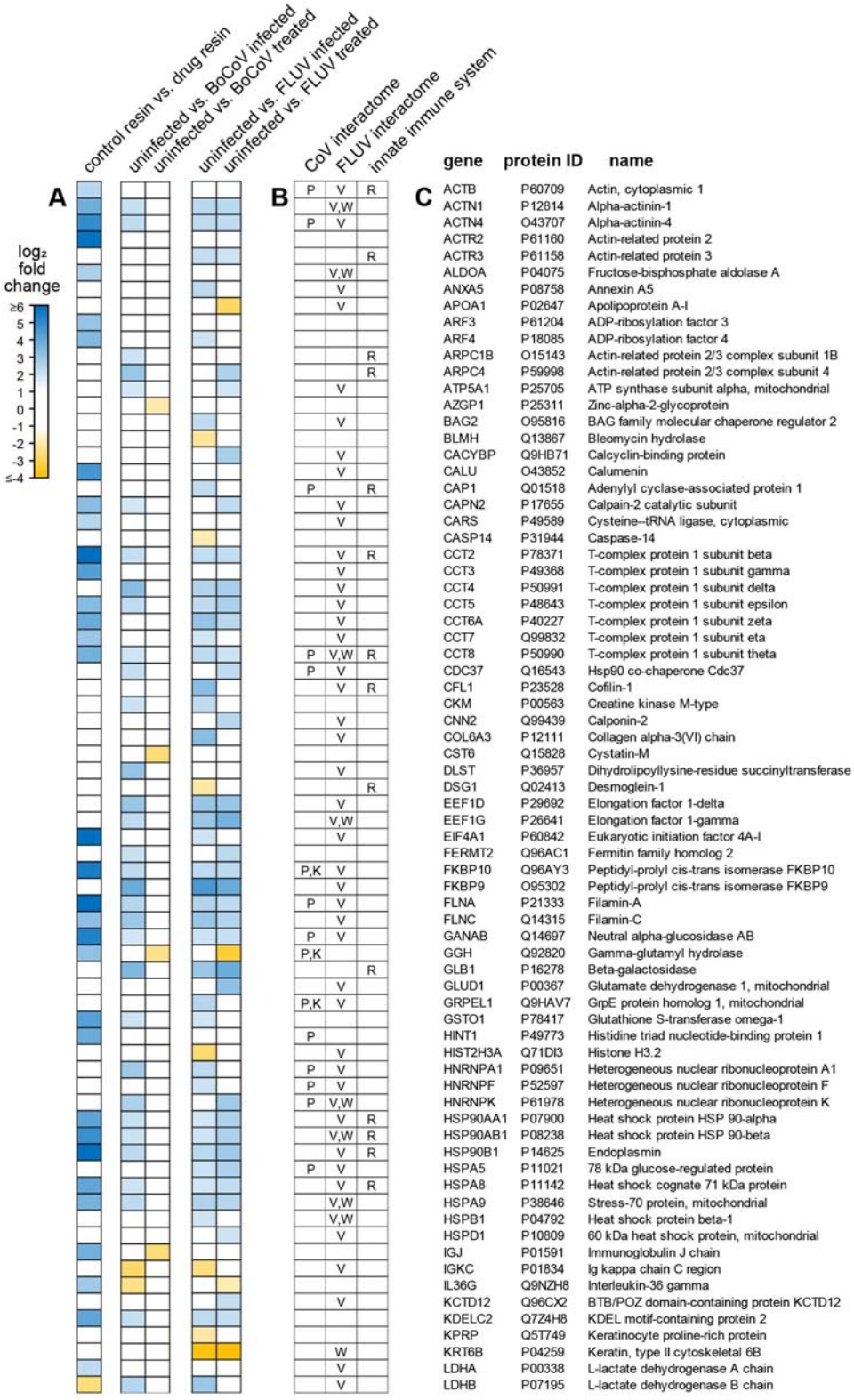

1182

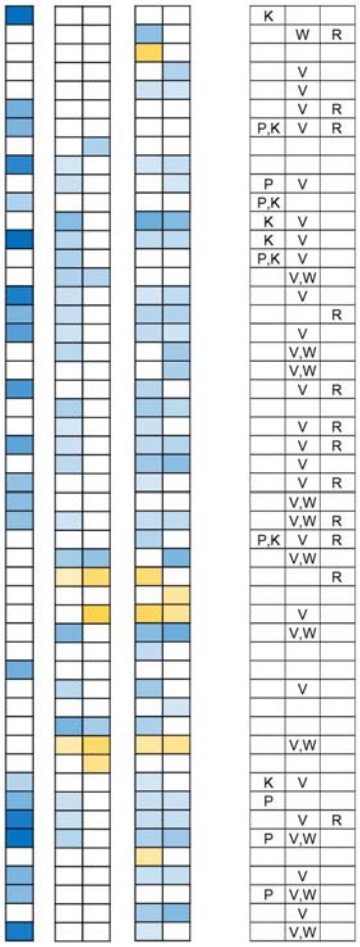

K			LGALS1	P09382	Galectin-1
	W	R	LGALS3	P17931	Galectin-3
			LOR	P23490	Loricrin
	V		MARCKS	P29966	Myristoylated alanine-rich C-kinase substrate
	V		MDH2	P40926	Malate dehydrogenase, mitochondrial
	V	R	MIF	P14174	Macrophage migration inhibitory factor
P,K	V	R	MYH9	P35579	Myosin-9
			NCCRP1	Q6ZVX7	F-box only protein 50
			NQO1	P15559	NAD(P)H dehydrogenase [quinone] 1
P	V		NUDC	Q9Y266	Nuclear migration protein nudC
P,K			NUTF2	P61970	Nuclear transport factor 2
K	V		P4HA1	P13674	Prolyl 4-hydroxylase subunit alpha-1
K	V		P4HB	P07237	Protein disulfide-isomerase
P,K	V		PABPC1	P11940	Polyadenylate-binding protein 1
	V,W		PDIA3	P30101	Protein disulfide-isomerase A3
	V		PDIA6	Q15084	Protein disulfide-isomerase A6
		R	PDXK	O00764	Pyridoxal kinase
	V		PLS3	P13797	Plastin-3
	V,W		PPIB	P23284	Peptidyl-prolyl cis-trans isomerase B
	V,W		PRDX3	P30048	Thioredoxin-dependent peroxide reductase, mitochondrial
	V	R	PRDX4	Q13162	Peroxiredoxin-4
			PRDX5	P30044	Peroxiredoxin-5, mitochondrial
	V	R	PRDX6	P30041	Peroxiredoxin-6
	V	R	PRKCSH	P14314	Glucosidase 2 subunit beta
	V		PRMT1	Q99873	Protein arginine N-methyltransferase 1
	V	R	PSAP	P07602	Prosaposin
	V,W		PSMA5	P28066	Proteasome subunit alpha type-5
	V,W	R	PSME1	Q06323	Proteasome activator complex subunit 1
P,K	V	R	RAB7A	P51149	Ras-related protein Rab-7a
	V,W		RCN1	Q15293	Reticulocalbin-1
		R	RNASE7	Q9H1E1	Ribonuclease 7
			SBSN	Q6UWP8	Suprabasin
	V		SERPINA12	Q8IW75	Serpin A12
	V,W		SERPINH1	P50454	Serpin H1
			SGSH	P51688	N-sulphoglucosamine sulphohydrolase
			TAGLN	Q01995	Transgelin
	V		TCP1	P17987	T-complex protein 1 subunit alpha
			TKT	P29401	Transketolase
			TMSB4X	P62328	Thymosin beta-4
	V,W		TPI1	P60174	Triosephosphate isomerase
			TPM3	P06753	Tropomyosin alpha-3 chain
K	V		UGGT1	Q9NYU2	UDP-glucose:glycoprotein glucosyltransferase 1
P			UGP2	Q16851	UTP--glucose-1-phosphate uridylyltransferase
	V	R	VCP	P55072	Transitional endoplasmic reticulum ATPase
P	V,W		VIM	P08670	Vimentin
			XP32	Q5T750	Skin-specific protein 32
	V		YWHAB	P31946	14-3-3 protein beta/alpha
P	V,W		YWHAE	P62258	14-3-3 protein epsilon
	V		YWHAQ	P27348	14-3-3 protein theta
	V,W		YWHAZ	P63104	14-3-3 protein zeta/delta

Supplementary Figure S3. Proteins corresponding to colored points in Figure 2 volcano plots ($|\log_2$ fold change$| > 1$ and p-value < 0.05), determined from MS-MS data analyzed by label free quantification with MaxQuant and LFQ-Analyst. (**A**) Fold change values illustrating the proteins that changed between compared conditions. (**B**) Known involvement in the CoV, FLUV, and innate immune system interactomes, with sources indicated. P, Perin-Cocon; K, Krogan; V, VirusMentha; W, Watanabe; R, Reactome. (**C**) Gene and protein identifiers.

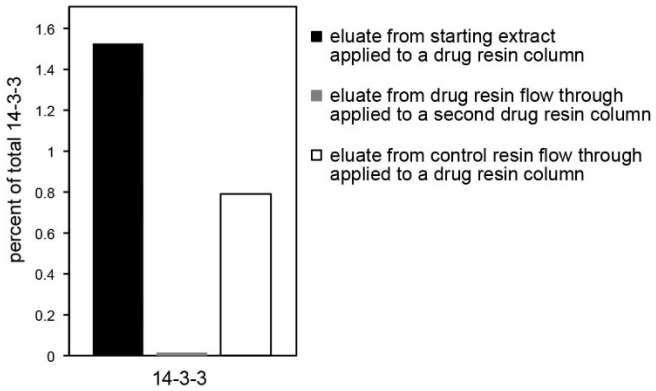

Supplementary Figure S4. Assembly machines represent a small subset of the total cellular abundance of their protein components, demonstrated here with eluates from a serial eDRAC experiment using a pig lung extract analyzed by SDS-PAGE and WB for direct drug binding protein 14-3-3. Representative data shown.

A

Criteria	Optimal	PAV-431	Comments
		Efficacy	
***In vitro* EC_{50}**	< 100 µM	0.025 µM	Excellent
***In vitro* CC_{50}**	> 5 µM	2.5 µM	OK
TI	> 50	100	Excellent
In vivo	Significant findings < 10 mg/kg PO		40% reduction in RSV titer in cotton rat lung; early analogs helped improve survival in coronavirus pig model
		Safety	
hERG (CV)	IC_{50} > 20 µM or x fold over [plasma] > 300	16.5 µM	Acceptable
Drug interactions	IC_{50} > 1 µM	CYP2C9 = 14.52 µM CYP3A4 = 30.6 µM	Good
Genetox	Ames is negative	Ames is negative	Good
		PK	
Bioavailability	%F > 30% PO/IV	F% = 58% IP (5 mg/kg)	Acceptable
Clearance	CL_{int} < 100, $T_{1/2}$ > 30 min in HLM/MLM, mouse $T_{1/2}$ > 3.5 hr (PO)	HLM = 40.38 min PigLM = 18.9 min Rat $T_{1/2}$ = 5 hr	$T_{1/2}$ in rats is good HLM is marginal
Lung exposure	Rat lung/plasma > 1	355 nM, IP after 2h	Good

B

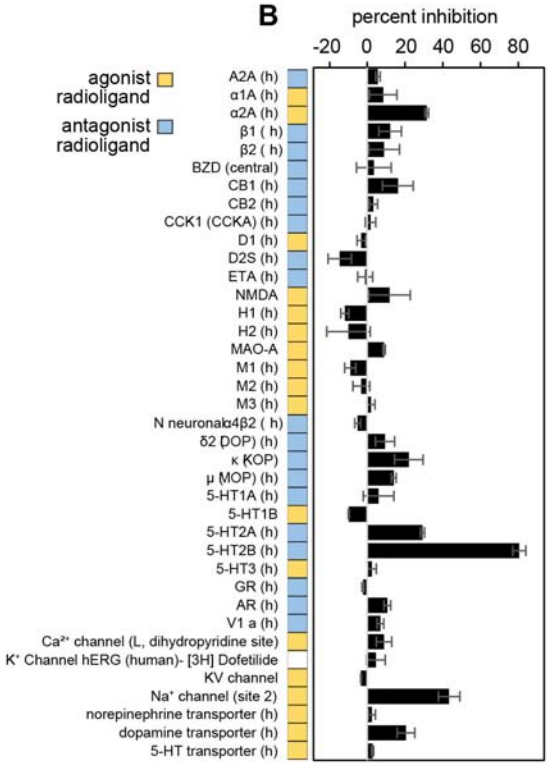

Supplementary Figure S5. Progression to a target product profile. (**A**) PAV-431 demonstrated a range of parameters that need to be fulfilled for clinical candidate nomination. (**B**) *In vitro* Cerep panel, a commercial screen for potential to bind to a broad panel of receptors, enzymes, and ion channels, reported as percent inhibition of control specific binding. PAV-431 was tested at 50µM, a concentration ~500x higher than antiviral EC_{50}. Data shown are the averages of replicates; error bars indicate standard error.

	EC_{50} FLUV	EC_{50} CoV	safe dose
PAV-431	< 25 nM	< 100 nM	5 mg/kg
PAV-471	< 10 nM	< 10 nM	1 mg/kg
PAV-104	< 10 nM	< 10 nM	15 mg/kg

Supplementary Figure S6. Summary of efficacy against FLUV A/WSN/33 in MDCK cells, efficacy against human coronavirus CoV229E in MRC-5 cells, and toxicology in BALB/c mice by intraperitoneal injection. Advanced analogs PAV-471 and PAV-104 both exhibit potent antiviral activity; PAV-104 is dramatically less toxic than PAV-471

Supplementary Tables

compound	molecular weight (g/mol)	log P	H-bond donors	H-bond acceptors	topological polar surface area (Å^2)
PAV-773	331.416	2.74	1	4	65.38
PAV-835	315.373	1.72	1	4	65.38
PAV-431	369.344	3.3	1	4	65.38
PAV-471	547.72	1.76	1	7	106
PAV-104	581.69	1.31	1	7	123.07

Table S1. Drug-like properties of compounds in the lead series progression to PAV-431 and beyond, including parameters related to Lipinski's "rule of five".

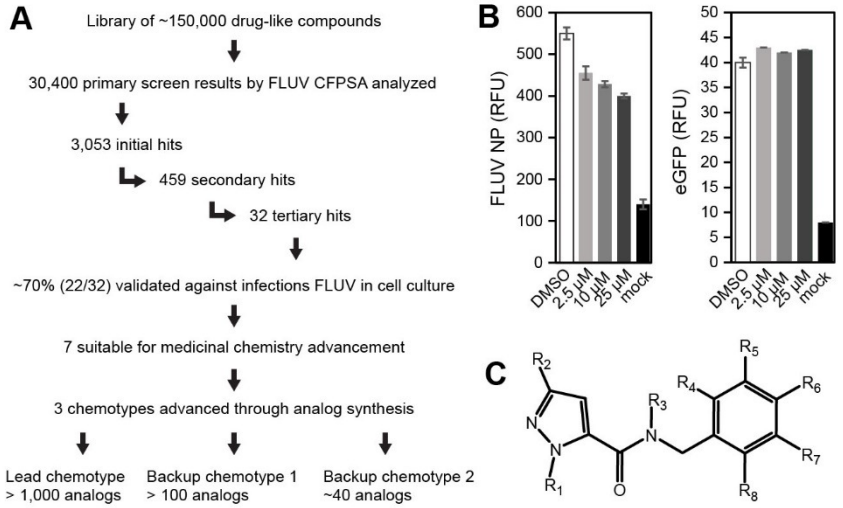

D

compound	R_1	R_2	R_3	R_4	R_5	R_6	R_7	R_8	EC_{90}(µM)
PAV-770	Me	t-Bu	H	O-CH_2-	CH_2-O-	H	F	H	1 - 3
PAV-868	Me	t-Bu	H	OMe	OMe	OMe	H	H	> 3
PAV-858	Me	t-Bu	H	OMe	H	OMe	OMe	H	> 3
PAV-772	Me	t-Bu	H	OMe	F	H	F	H	3
PAV-736	CH_2CH_2OH	t-Bu	H	OMe	OMe	H	H	H	> 3
PAV-869	Me	t-Bu	H	OPr	OMe	H	H	H	> 3
PAV-773	Me	t-Bu	H	OMe	OMe	H	H	H	< 1
PAV-1866	Me	t-Bu	Me	OMe	OMe	H	H	H	> 3
PAV-834	Me	Me	H	OMe	OMe	H	H	H	3
PAV-854	Me	Cy-hex	H	OMe	OMe	H	H	H	> 1
PAV-530	Me	iPr	H	OMe	OMe	H	H	H	1
PAV-835	Me	cyPr	H	OMe	OMe	H	H	H	< 1
PAV-895	Me	cyPr	H	OMe	Me	H	H	H	2
PAV-039	Me	cyPr	H	OMe	OMe	H	H	F	1
PAV-896	Me	cyPr	H	Me	OMe	H	H	H	1.5
PAV-700	Me	cyPr	H	Cl	OMe	H	H	H	2
PAV-235	Me	cyPr	H	F	OMe	H	H	H	0.2
PAV-944	Me	cyPr	H	OMe	CF_3	H	H	H	0.2
PAV-901	Me	cyPr	H	CF_3	OMe	H	H	H	0.3
PAV-671	Me	cyPr	H	H	Cl	OCF_3	H	H	0.05
PAV-774	Me	cyPr	H	Cl	OCF_3	H	H	H	0.2
PAV-431	Me	cyPr	H	OMe	OCF_3	H	H	H	< 0.1
PAV-528	Me	cyPr	H	$OCHF_2$	$OCHF_2$	H	H	H	< 0.1
PAV-877	Me	cyPr	H	H	Me	$OCHF_2$	Me	H	> 2

Figure 1. Mueller-Schiffmann et al.

Legend to Figure 1. A. Output of the moderate throughput CFPSA screen involving FLUV nucleoprotein, culminating in three chemotypes validated against infectious virus, one of which was most extensively advanced and is presented here. B. Initial hit (PAV-770) of this chemotype in the plate screen showing dose-dependent titration of FLUV RFUs (left, reflecting inhibition of np multimerization/assembly) with no effect on eGFP RFUs (right, reflecting inhibition of protein synthesis). C. Markush structure of the lead series. D. Initial structure-activity relationship based on assessment of FLUV infectivity in MDCK cells treated with these analogs.

Figure 2. Mueller-Schiffmann et al.

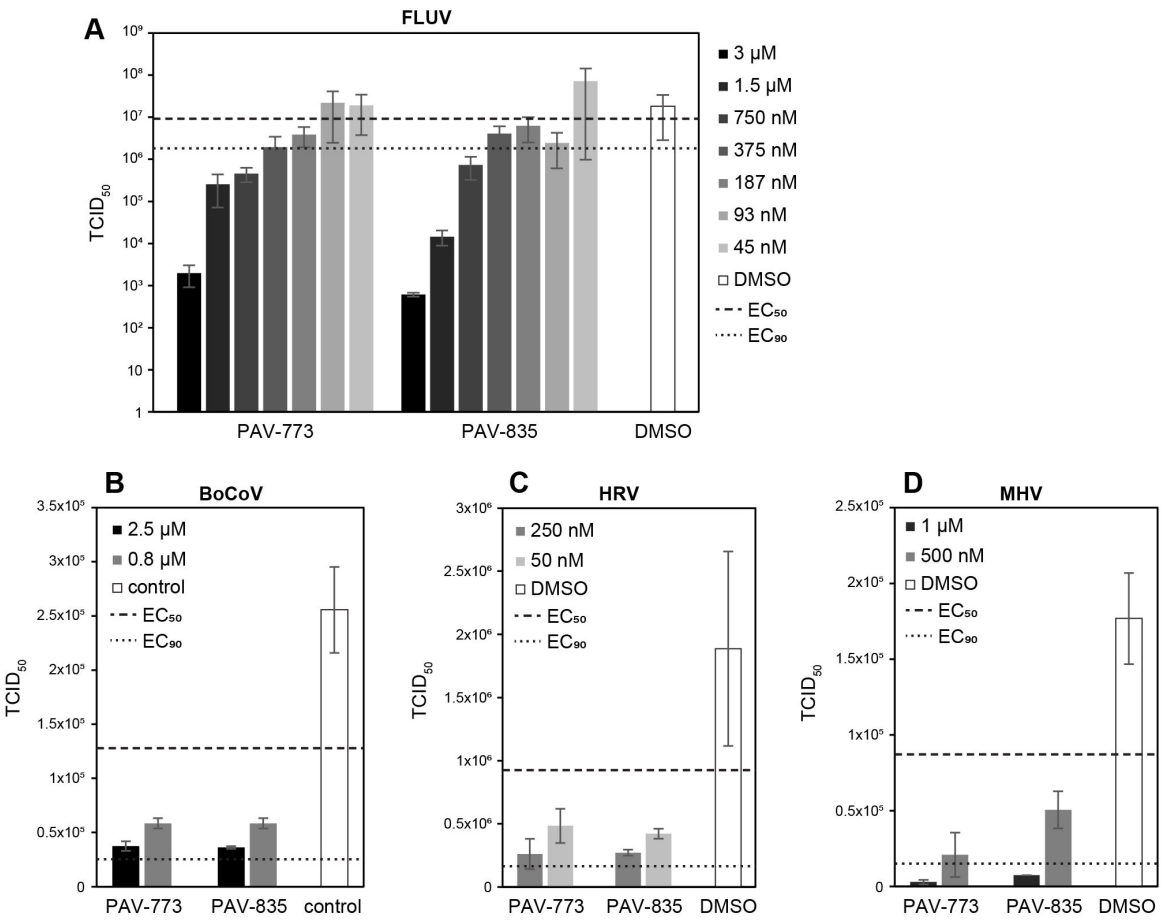

Legend to Figure 2. Assessment of pan-respiratory antiviral activity of early compounds PAV-773 and PAV-835, determined by $TCID_{50}$. Data shown are the averages of three biological replicates; error bars indicate standard error; DMSO is included as the vehicle control. (**A**) FLUV A/WSN/33 in MDCK cells. (**B**) BoCoV (BRCV-OK-0514-2) in HRT-18G cells, (**C**) HRV-16 in H1-HeLa cells, (**D**) MHV-68 in BHK-2 cells. Dashed line is the EC_{50}. Dotted line is the EC_{90}.

Figure 3. Mueller-Schiffmann et al.

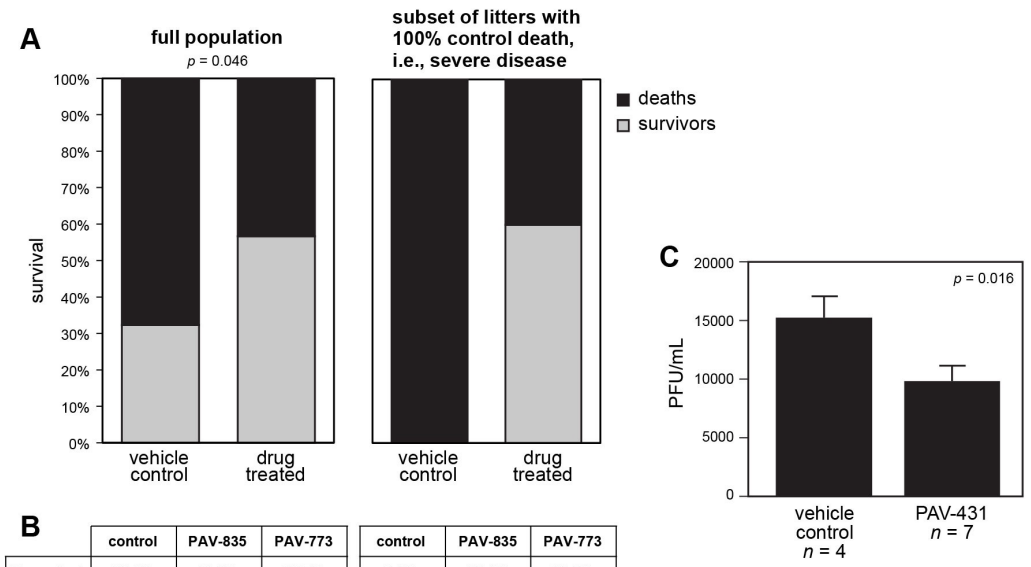

B

	control	PAV-835	PAV-773	control	PAV-835	PAV-773
% survival	32.3%	56.7%	56.7%	0.0%	57.1%	66.7%
survivors	10	17	17	0	8	10
deaths	21	13	13	15	7	5

Legend to Figure 3. Early analogs validated in animal efficacy trials. (**A-B**) PEDV pig trial, evaluated by survival. (**A**) Assembly modulator compounds demonstrated efficacy against both mild and severe disease. As PAV-773 and PAV-835 showed equal efficacy, they have been combined (Fisher exact test $p = 0.046$). The left panel shows percent survival for all animals in the study. The right panel shows the subset of litters in which all control animals (treated with vehicle only) died. (**B**) Breakdown of survival for PAV-773 and PAV-835 separately for both the total population and the severe disease subset, where $p = 0.002$ and $p = 0.004$, respectively. This breakdown reveals the compounds to be as potent against mild disease (groups in which there were vehicle-only survivors) as in severe disease (groups in which there were no vehicle-only survivors). (**C**) RSV cotton rat trial, evaluated by day 5 lung viral titer determined by plaque assay. A significant drop in viral titer was observed with PAV-431 treatment (unpaired *t*-test $p = 0.016$). Data shown are averages; error bars indicate standard error.

Figure 4. Mueller-Schiffmann et al.

A

cell line	virus (family)	PAV-431 EC_{50}
MDCK	influenza A/WSN/33 (*Orthomyxoviridae*)	25 nM
MDCK	swine influenza virus SIV/SK WT (*Orthomyxoviridae*)	25 nM
GBK	bovine coronavirus (*Coronaviridae*)	50 nM
Vero E6	SARS-CoV-2 WA1/2020 (*Coronaviridae*)	100 nM
HEp2	respiratory synctial virus strain A-2 (*Paramyxoviridae*)	< 25 nM
HSAEC1-KT	Nipah virus rNiV-ZsG (*Paramyxoviridae*)	≤ 50 nM
A549	adenovirus serotype 5 strain adenoid 65 (*Adenoviridae*)	< 100 nM
H1-Hela	human cytomegalovirus strain AD69 (*Herpesviridae*)	25 nM
H1-Hela	human rhinovirus 16 (*Picornaviridae*)	< 20 nM
MNA	rabies virus CVS-11 (*Rhabdoviridae*)	> 400 nM

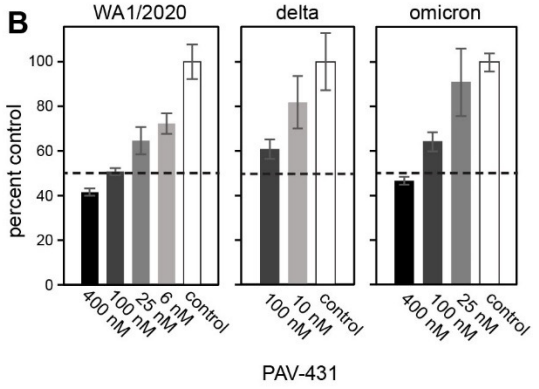

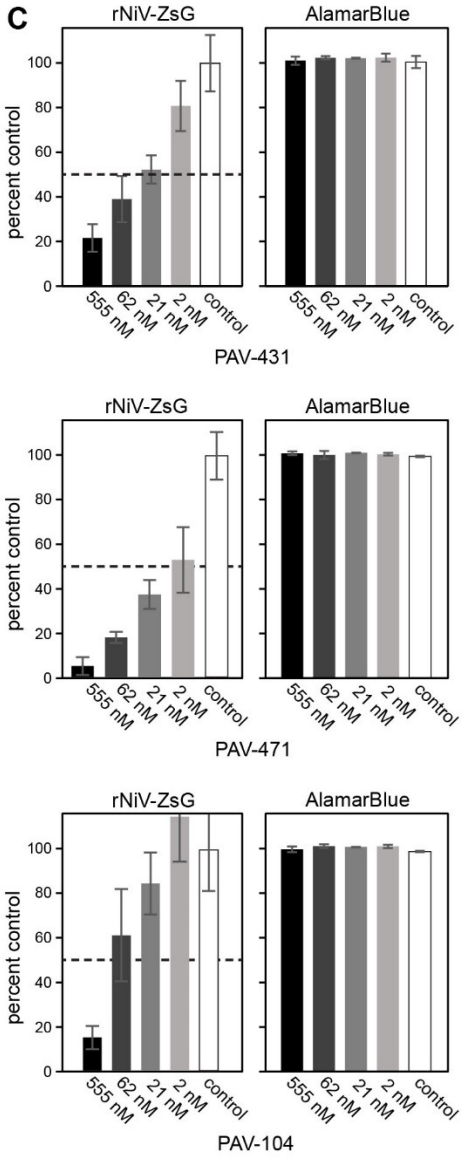

Legend to Figure 4. Pan-respiratory antiviral activity. (**A**) Efficacy of PAV-431 against each respiratory viral family in cell culture. **(B)** Dose-dependent antiviral activity of PAV-431against multiple SARS-CoV-2 strains: (WA1/2020, lineage A) in Vero E6 cells, determined by plaque assay, delta variant (lineage B.1.617.2) and omicron variant (lineage B.A.1) in Calu-3 cells determined by qPCR measurement of the SARS-CoV-2 E gene and/or $TCID_{50.}$ Data shown are the averages of three biological replicates; error bars indicate standard error; DMSO is included as the vehicle control. **(C)**. Dose-dependent activity of PAV-431 and advanced analogs PAV-471 and PAV-104 against Nipah virus of the *Paramyxoviridae* family in primary-like human small airway epithelial cells (HSAEC1-KT)(Lo et al., 2014; Welch et al., 2020). Alamar Blue assessment of cytotoxicity shows no toxicity up to 5uM tested in 5mM glucose-supplemented minimum essential medium, so all therapeutic indices > 100.

Figure 5. Mueller-Schiffmann et al.

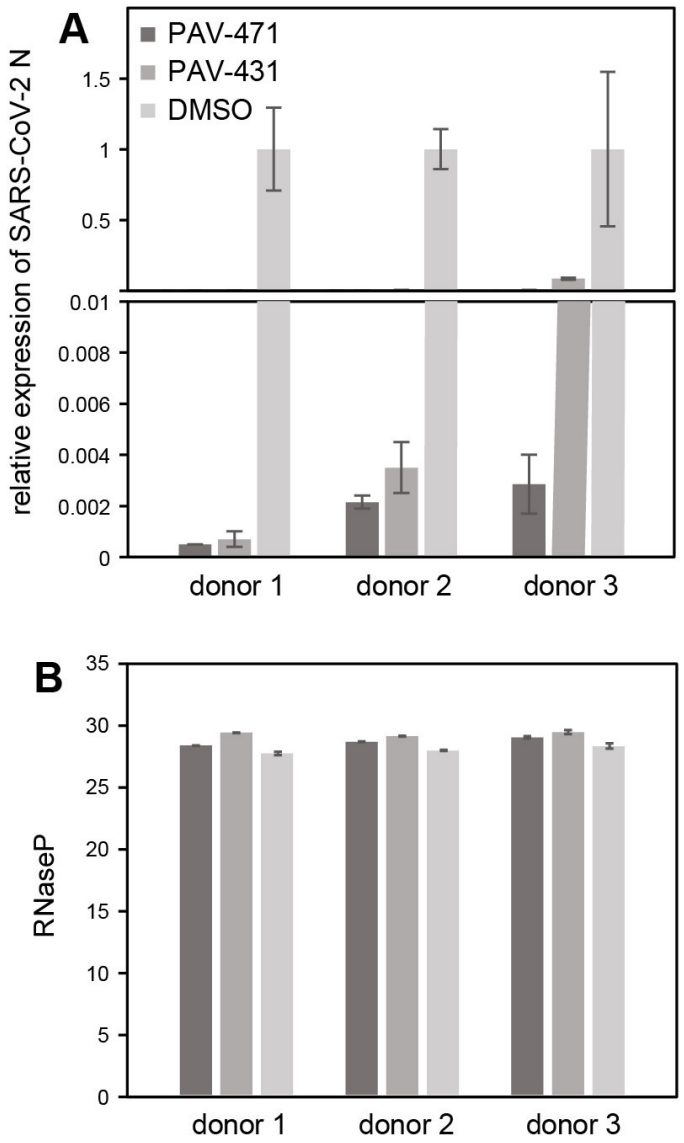

Legend to Figure 5. A. Assembly modulator compounds inhibit SARS-CoV-2 (gamma variant, lineage P.1) replication in primary human airway epithelial cells grown at an air-liquid interface, determined by qPCR measurement of the SARS-CoV-2 N gene. Data shown are the averages of two biological replicates; error bars indicate standard error; DMSO is included as the vehicle control. B. No significant toxicity was observed by assessment of levels of RNase P.

Figure 6. Mueller-Schiffmann et al.

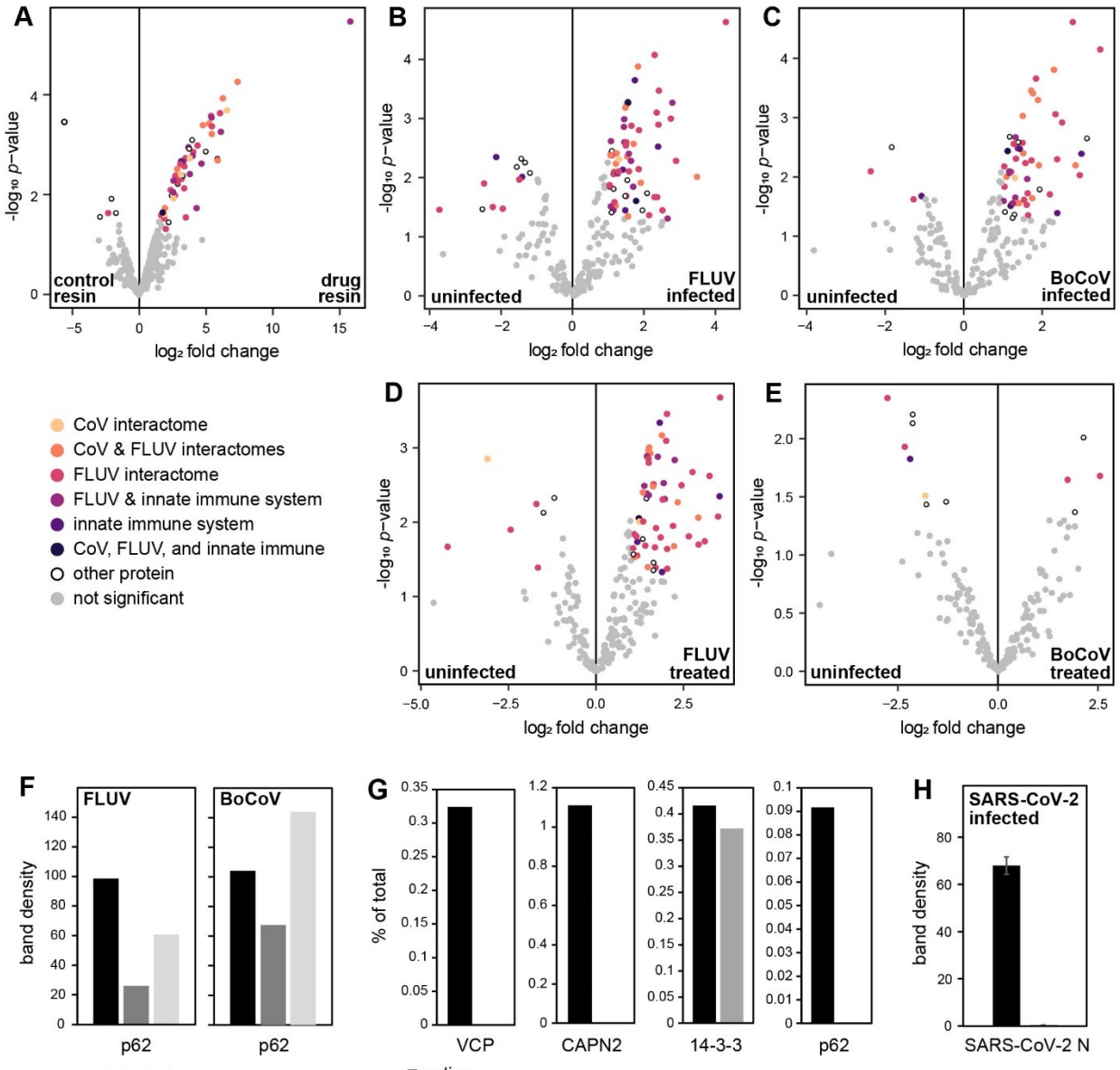

Legend to Figure 6. Drug target is a host multi-protein complex modified by viral infection and restored with drug treatment. (**A-E**) Volcano plots visualizing the protein composition of the target complex determined by MS-MS on triplicate eDRAC eluates from extracts of MRC-5 cells that were either uninfected, infected with FLUV or BoCoV, or infected and treated with PAV-431. Significant proteins ($|\log_2$ fold change$| > 1$ and p-value < 0.05) are colored based on their known involvement in the CoV, FLUV, and innate immune system interactomes and listed in Supplementary Figure S3. (**A**) Comparison between control resin and PAV-431 drug resin demonstrates drug specificity of the target complex. (**B-C**) Infection with FLUV (B) or BoCoV (C) modifies the target complex. (**D-E**)**,** Treatment with PAV-431 restores the target to the uninfected state, partially for FLUV (D) and almost completely for BoCoV (E). (**F**) eDRAC eluates from MRC-5 cells (left) and HRT-18G cells (right), uninfected or infected with either FLUV (left) or BoCoV (right), analyzed by SDS-PAGE and WB for target component p62. In both cases, viral infection resulted in a diminution of p62, which was restored by treatment with PAV-431 (right) and PAV-818 (left). (**G**) Crosslinked eDRAC eluates from pig lung extract co-precipitated under native or denaturing conditions and analyzed by SDS-PAGE and WB for target components p62, VCP, CAPN2, and 14-3-3. Presence under both conditions identifies 14-3-3 as the direct drug binding protein, while loss under denaturing conditions identifies the others as more distal components of the complex associated with the drug indirectly via other proteins in the complex that are associated with the direct-binding protein 14-3-3. (**H)** SARS-CoV-2 infected an PAV-431-treated cell lysate subjected to PAV-431 photocross-linking and streptavidin precipitation under non-denaturing conditions. A-E and H show the statistical significance of the findings, F and G show representative individual experiments. Drug concentration for treatment of infected cells in H was 100nM.

Figure 7. Mueller-Schiffmann et al.

A

		PAV-773			PAV-835		PAV-431			PAV-471		PAV-104		
mouse maximum tolerated dose	safe dose route-dosage (mg/kg)	-	IP-5	-	-	IP-1	-	IP-5	-	-	IP-1	-	IP-15	PO-50
	toxic dose route-dosage (mg/kg)	-	IP-15	-	-	IP-15	-	IP-10	-	-	IP-2	-	IP-20	PO-250
repeat dose toxicology [a] mouse 10 day [b] rat 7 day	route-dosage (mg/kg)	-	IP-5[a]	-	-	IP-1[a]	-	IP-2[a]	-	-	-	-	-	PO-50[b]
	body weight, clinical signs, histopathology, clinical parameters	-	NAD/ NSSD	-	-	NAD/ NSSD	-	NAD/ NSSD	-	-	-	-	-	NAD/ NSSD
rat PK [c] mouse	route-dosage (mg/kg)	IV-1[c]	IP-5[c]	PO-5[c]	IV-0.2	IP-1	IV-1	IP-5	PO-5	IV-0.2	IP-1	IV-1	IP-5	PO-20
	AUC_{last} (nM.h)	2287	733	253	428	1043	831	2464	low conc.	108	371	543	2510	3247
	AUC_{inf} (nM.h)	ND	ND	ND	428	1047	926	2499		135	387	559	2656	3620
	C_{max} (nM)	ND	1035	51	1608	2842	685	793		152	550	1379	2243	1417
	T_{max} (h)	ND	0.08	4	0.03	0.08	0.08	0.25		0.08	0.25	0.08	0.25	0.5
	$t_{½}$ (h)	ND	ND	ND	0.5	0.4	12	5		4	2	2	7	9
	CL (mL/min)	1.3	-	-	25	-	49	-		45	-	51	-	-
	V_z (L/Kg)	13.3	-	-	0.5	-	32	-		12	-	4	-	-
	F (%)	-	7	2.2	-	49	-	59		-	69	-	95	32
rat uptake [c] mouse timepoints: [d] 5 min [e] 30 min [f] 1 hour [g] 2 hours [h] 24 hours	route-dosage (mg/kg)	-	IP-5[c]	-	-	IP-1[c]	-	IP-5	-		IP-1	-	IP-5	PO-20
	concentration in lungs (nM)	-	866[d] 109[f]	-	-	98[e] 5[g]	-	1224[e] 355[g]	-	-	739[e] 175[g]	-	160[e] 485[g]	306[e] 113[g] 53[h]
	concentration in brain (nM)	-	2148[d] 169[f]	-	-	178[e] 20[g]	-	1416[e] 479[g]	-	-	334[e] 69[g]	-	17[e] BLOQ[g]	26[e] BLOQ[g] BLOQ[h]
	concentration in plasma (nM)	-	1657[d] 250[f]	-	-	181[e] 18[g]	-	834[e] 333[g]	-	-	265[e] 40[g]	-	397[e] 261[g]	1011[e] 371[g] 22[h]

B

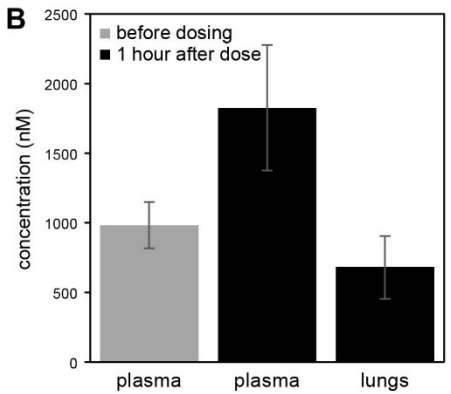

Legend to Figure 7. Pharmacokinetic and toxicological assessment of the lead series in BALB/c mice and Sprague Dawley rats. (**A**) Summary of results. IV, intravenous; IP, intraperitoneal; PO, per oral; PK, pharmacokinetics; AUC_{last}, area under the curve from time zero to the last quantifiable concentration; AUC_{inf}, area under the curve vs. time curve extrapolated to infinity; C_{max}, peak plasma concentration; T_{max}, time of peak concentration observed; $t_{1/2}$, terminal half-life; CL, steady-state clearance; V_z, volume of distribution; F, fraction bioavailability; NAD, no abnormality detected; NSSD, no significant statistical difference; BLOQ, below level of quantification; ND, not determined. Pharmacokinetic parameters were determined using WinNonlin software. **(B)** PAV-104 levels following acute repeat dose toxicology evaluation in Sprague Dawley rats with a daily oral dose of 50 mg/kg for 7 days. Trough plasma levels exceed EC_{50} by ~100 fold. Data shown are the averages of 5 animals; error bars indicate standard deviation.

Figure 8. Mueller-Schiffmann et al.

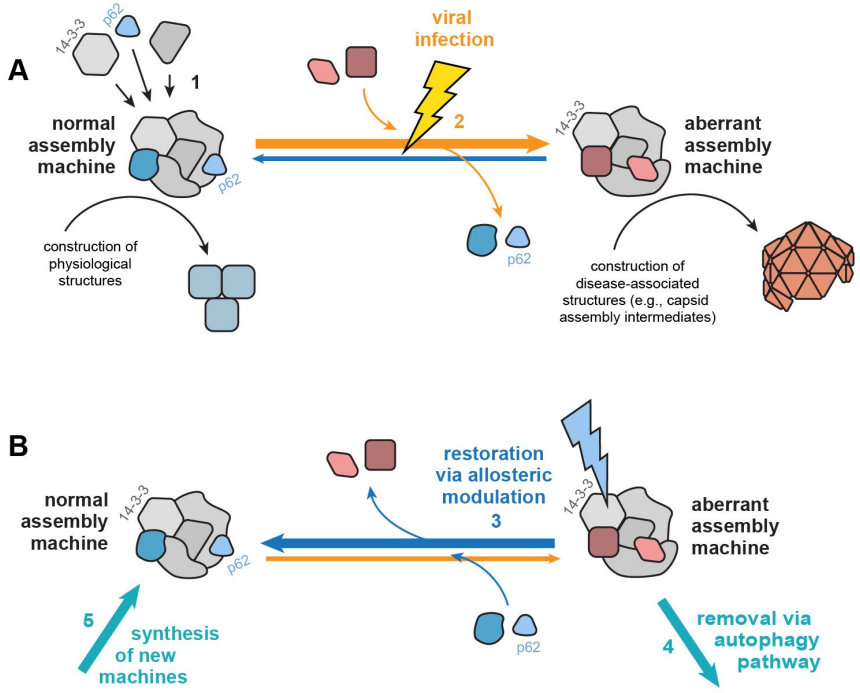

Figure 8. Cartoon summarizing our working hypothesis on assembly modulation therapeutics. (**A**) Normal assembly machines are transient host multi-protein complexes that come together to carry out various events involved in the construction of physiological structures and maintenance of homeostasis (1). Viruses have evolved to co-opt the assembly machines of their hosts to meet their own needs, presumably through signaling pathway manipulation and/or allosteric site modulation (2). This results in the formation of aberrant assembly machines that do something they are not supposed to do (e.g. build a viral capsid) and perhaps fails to do something they are supposed to do (e.g. inform innate immunity that the cell is under viral attack) due to loss of autophagy regulator p62. The former action is reflected as viral replication and the latter action is reflected in the failure of autophagic innate immune defense. Both consequences manifest as disease and their molecular basis is the normal to aberrant change in assembly machine composition. (**B**) Treatment with assembly modulators results in elimination of aberrant assembly machines and restoration of normal assembly machines. This could be a result of either direct action on the allosteric site (e.g. affecting protein-protein interactions such that the normal assembly machine is stabilized) or indirectly by activation of autophagy to destroy the aberrant assembly machines (4) followed by homeostatic feedback repopulation of normal assembly machines (5).

Table 1. Mueller-Schiffmann et al.

		percent reduction in infection
Oseltamivir	passage 0 at 30 μM	91
	passage 7 at 30 μM	21.4
PAV-835	passage 0 at 3 μM	98.9
	passage 7 at 3 μM	91.9
PAV-333	passage 0 at 3 μM	94.5
	passage 7 at 3 μM	92.5

Legend to Table 1. Evidence for a barrier to resistance development. MDCK cells were infected with FLUV (A/WSN/33) in the presence of Oseltamivir (935 nM to 30 μM), PAV-835 (93.5 nM to 3 μM), or PAV-333 (93.5 nM to 3 μM). From passage to passage, drug concentrations were increased over the indicated ranges to encourage selection for resistance mutants. An initially Oseltamivir-sensitive FLUV strain became largely resistant after passage 7. In contrast, the two assembly modulator compounds PAV-835 and PAV-333 showed minimal loss of drug sensitivity.